Geophysical Journal International

Geophys. J. Int. (2024) **240,** 1079–1095
Advance Access publication 2024 December 05
GJI Geomagnetism and Electromagnetism

https://doi.org/10.1093/gji/ggae432

Paleomagnetic inclinations and relative paleointensity variations during the upper Aptian to middle Albian in Sergipe-Alagoas Basin, South Atlantic Ocean (NE Brazil)

Raquel Gewehr de Mello,[1] Jairo F. Savian,[1,2] Gerson Fauth,[3] Fabio Florindo,[4] Anita Di Chiara,[4] Sara Satolli,[5] Henrique B. Roisenberg,[6] Carolina G. Leandro,[1] Camila Trindade Lopes,[2] Caroline A. Pontel,[1] Everton Frigo,[7] Alessandra Santos,[3] Simone Baecker-Fauth,[3] Mauro D. R. Bruno,[3] Rodrigo M. Guerra,[3,8] Guilherme Krahl,[3] Karlos G. D. Kochhann,[3] Fernando M. Lopes,[3] Ricardo I. F. Trindade[9] and Lilla Spagnuolo[4]

[1] *Programa de Pós-Graduação em Geociências, Universidade Federal do Rio Grande do Sul, Av. Bento Gonçalves* 9500, 91501-970 *Porto Alegre, RS, Brazil. E-mail:* raquel_evenstar@hotmail.com
[2] *Instituto de Geociências, Universidade Federal do Rio Grande do Sul, Porto Alegre, Brazil*
[3] *Instituto Tecnológico de Paleoceanografia e Mudanças Climáticas (itt Oceaneon), Unisinos, São Leopoldo, Brazil*
[4] *Istituto Nazionale di Geofisica e Vulcanologia, Rome, Italy*
[5] *Dipartimento di Ingegneria e Geologia, Università 'G. d'Annunzio' di Chieti-Pescara, Italy*
[6] *Dipartimento di Scienze - Università Degli Studi Roma Tre, Italy*
[7] *Universidade Federal do Pampa, Caçapava do Sul, Brazil*
[8] *Museu Itinerante de Ciências Naturais, Carlos Barbosa, Brazil*
[9] *Instituto de Astronomia, Geofisica e Ciências Atmosféricas, Universidade de São Paulo, São Paulo, Brazil*

Accepted 2024 December 2. Received 2024 November 26; in original form 2024 June 20

SUMMARY

During the Jurassic and Early Cretaceous, Earth's magnetic field experienced a high frequency of polarity reversals. This hyperactivity period is followed by a ∼38 Myr prolonged period of stable normal polarity from the Aptian until the Santonian, known as the Cretaceous Normal Superchron (CNS; chron C34n, from 121.4 to 83.65 Ma). However, the CNS might have been characterized by more variability than previously thought, but the current database is uneven in its spatial and temporal distribution. In this study, we integrate paleomagnetic and biostratigraphic data from the SER-03 sedimentary core, drilled onshore in the Sergipe-Alagoas Basin, NE Brazilian margin, South Atlantic Ocean. The 183-m cored interval spans 5.2 Myr (114.7–109.5 Ma), including the Aptian–Albian transition. It records the evolution from restricted marine settings to the complete opening of the South Atlantic Ocean. Magnetic remanence and rock magnetic parameters, such as magnetic susceptibility, anhysteretic remanent magnetization and isothermal remanent magnetization, were measured. Rock magnetic analyses indicated that primary magnetizations were preserved throughout the interval, with detrital magnetite identified as the primary magnetic carrier, predominantly in the pseudo-single domain and low-coercivity states. Normalizations by χ, $\mathrm{ARM}_{15\mathrm{mT}}$ and $\mathrm{IRM}_{15\mathrm{mT}}$ were used to determine relative paleointensity curves and were compared to the curve resulting from the pseudo-Thellier method. The SER-03 relative paleointensity record shows marked changes in both intensity and inclination. Inclination instability results are comparable with those found in volcanic rocks from surrounding the region. The high-resolution SER-03 magnetic record revealed that the field variability was higher than expected during the CNS, but remaining substantially lower than during other periods, such as the late Jurassic. The new SER-03 can serve as a dating and correlation tool for coeval records.

Key words: Magnetic mineralogy and petrology; Magnetostratigraphy; Palaeomagnetic secular variation.

1 INTRODUCTION

Geomagnetic observatories and satellites have been the primary sources of Earth's magnetic field data (e.g. Whaler & Holme 2011). These direct measurements enable the observation of a rapid decrease in the geomagnetic field intensity (Hulot *et al.* 2002; Pavón-Carrasco & De Santis 2016; Brown *et al.* 2018) and the investigation of Earth's interior dynamics and its evolution over time and space (e.g. Aubert *et al.* 2010), primarily through numerical simulations (e.g. Glatzmaier & Roberts 1995; Lhuillier & Gilder 2013; Aubert & Finlay 2019). During the geological past, Earth's magnetic field variations are investigated through indirect measurements from geological archives (e.g. GEOMAGIA50 data set, Brown *et al.* 2015a; MagIC database, https://earthref.org/MagIC/; or Latin-American Paleomagnetic Online Database (LAPOD), Rodríguez-Trejo *et al.* 2024), displaying a sequence of magnetic polarity reversals which are intrinsic characteristics of the geodynamo, influenced by long-term changes in core heat flow and heat flux patterns across the core–mantle boundary (Glatzmaier *et al.* 1999). In general, directional and relative paleointensity data extracted from continuous sedimentary archives significantly contribute to our comprehension of past geomagnetic field variations (e.g. Meynadier *et al.* 1992; Guyodo & Valet 1999; Brown *et al.* 2015a, b). Nevertheless, very few studies provide an uninterrupted record of field changes for time intervals older than 2.0 Ma (e.g. Donadini *et al.* 2009; Cromwell *et al.* 2018; Panovska *et al.* 2019; Valet *et al.* 2020) and none of these records is in the Southern Hemisphere. Such biased and incomplete data set results in our poor understanding of, for instance, geodynamo processes within Earth's interior responsible for polarity changes.

Here, to fill this gap, we focus on the he Aptian–Albian interval in the Early Cretaceous. This period is characterized by notable paleoclimatic, palaeoceanographic and paleogeographic transformations (e.g. Leckie *et al.* 2002; Huber & Leckie 2011; Huber *et al.* 2011), alongside a stable normal polarity of the Earth's magnetic field, referred to as the Cretaceous Normal Polarity Superchron or Cretaceous Normal Superchron (CNS). This interval is also informally designated as the Cretaceous quiet zone, as observed in ocean-floor magnetic anomaly profiles by Helsley & Steiner (1968). The CNS has been investigated using paleomagnetic methods worldwide (e.g. Cronin *et al.* 2001; Di Chiara *et al.* 2021; Zhang *et al.* 2021; Liu *et al.* 2024) and it corresponds to an extended normal polarity Chron, C34n, spanning from 121.4 to 83.6 Myr (∼38.0 Myr, e.g. Gradstein *et al.* 2020; Olierook *et al.* 2020). Essentially, the CNS is an anomalously prolonged period of stable magnetic conditions. Hence, it serves as a valuable tool for understanding Earth's geodynamo processes, with its stability attributed to the thermal effects of mantle activity in the outer core (e.g. Helsley & Steiner 1968; McFadden & Merril 1984; Aubert *et al.* 2010; Biggin *et al.* 2012, 2015; Bono *et al.* 2019).

Before the onset of the CNS, the Jurassic period was characterized by high-rates of polarity reversals (Jurassic hyperactivity period, e.g. Franco *et al.* 2019; Kulakov *et al.* 2019). However, the debate persists regarding variations in geomagnetic field intensities throughout the CNS (e.g. Tarduno 1990; Cronin *et al.* 2001; Granot *et al.* 2012; Di Chiara *et al.* 2021). One point of contention arises from magnetic anomalies data (Granot *et al.* 2012). Deep-tow magnetic profiles in the Central Atlantic Ocean suggest the presence of two anomalous periods within the CNS with higher intensity values around 108 Ma and lower values around 92.0 Ma. However, these anomalies are not consistently identified in other volcanic or sedimentary records (e.g. Tarduno 1990; Cronin *et al.* 2001; Granot *et al.* 2012). Hence, new detailed paleomagnetic studies of sedimentary sequences from South America would contribute toward the possible identification of such anomalies and their understanding, offering valuable insights into this issue.

In this study, we provide high-resolution magnetic and paleoenvironmental records across the Aptian-Albian transition from core SER-03, drilled in the onshore segment of the Sergipe-Alagoas Basin, northeastern Brazil, western tropical South Atlantic Ocean (Fauth *et al.* 2021). This interval within the basin is records (in the Riachuelo Formation) the evolution from restricted marine sequences to the complete opening of the South Atlantic Ocean. Moreover, the area holds economic relevance due to its substantial contributions to oil and gas production (Koutsoukos, Mello & Azambuja and Filho 1991a; Koutsoukos *et al.* 1991b; Mello & Katz 2000). This contribution is based on previous research on the SER-03 core that demonstrated stable geomagnetic directions after alternating field (AF) demagnetization (Fauth *et al.* 2021; 2022).

The new directional and relative paleointensity records at core SER-03 are integrated with previous biostratigraphic and cyclostratigraphic studies, which indicate ages ranging from 109.5 to 114.7 Ma (Fauth *et al.* 2022), thus providing the opportunity to explore the behaviour of the geomagnetic field during the CNS and serving as a correlation tool for coeval basins.

2 GEOLOGICAL SETTING

The Sergipe-Alagoas Basin is well-known for its economic relevance in oil and gas production and hosts the most expanded marine Cretaceous sequence among the South Atlantic basins (Fig. 1a; Fauth *et al.* 2021). Core SER-03 (10°46′51.03" S, 37°14′53.95" W) was drilled in the onshore portion of the Sergipe-Alagoas Basin, near the town of Laranjeiras (Figs 1a and b). The core spans a total length of 200.1 m and achieved a recovery rate of 87.7 per cent (Fig. 1c; Fauth *et al.* 2021).

The continuous record from restricted marine conditions in the Early Cretaceous to open marine conditions in the late Aptian within the Riachuelo Formation, attributed to the Gondwana breakup (Fauth *et al.* 2021, 2022; Luft-Souza *et al.* 2022), marks the onset of the drift phase of tectono-sedimentary evolution. In Sergipe-Alagoas Basin, this phase comprises a 2800 m thick sedimentary package within the Sergipe Group, subdivided into the Angico, Maruim and Taquari interfingered members. It is mainly characterized by mixed calcareous and siliciclastic sediments deposited in a shelf environment, with an age range spanning the Aptian–Albian interval, based on ammonite, planktonic foraminifers and calcareous nannofossil biostratigraphy (Schaller 1969; Bengtson 1983; Koutsoukos *et al.* 1991a, b; Feijó 1994, 1996; Bengtson *et al.* 2018; Fauth *et al.* 2021, 2022; Luft-Souza *et al.* 2022).

The Angico Member represents fan delta deposits composed of mixed calcareous-siliciclastic sediments, predominantly deposited on the basin's margin and on lowered blocks. The Maruim Member consists of grainstones and oolitic/oncolitic packstones deposited on a carbonate platform, indicative of areas with reduced input of sedimentary terrigenous sediments. The Taquari Member recorded lagoonal environments on the outer shelf, characterized by the deposition of mudstones and wackestones (Schaller 1969; Cainelli *et al.* 1987; Campos Neto *et al.* 2007). Core SER-03 spans the Angico Member and is primarily composed of fine-grained sedimentary rocks such as shales, marls and packstones. Intermittent layers of dark grey shales occur (Fauth *et al.* 2021, 2022).

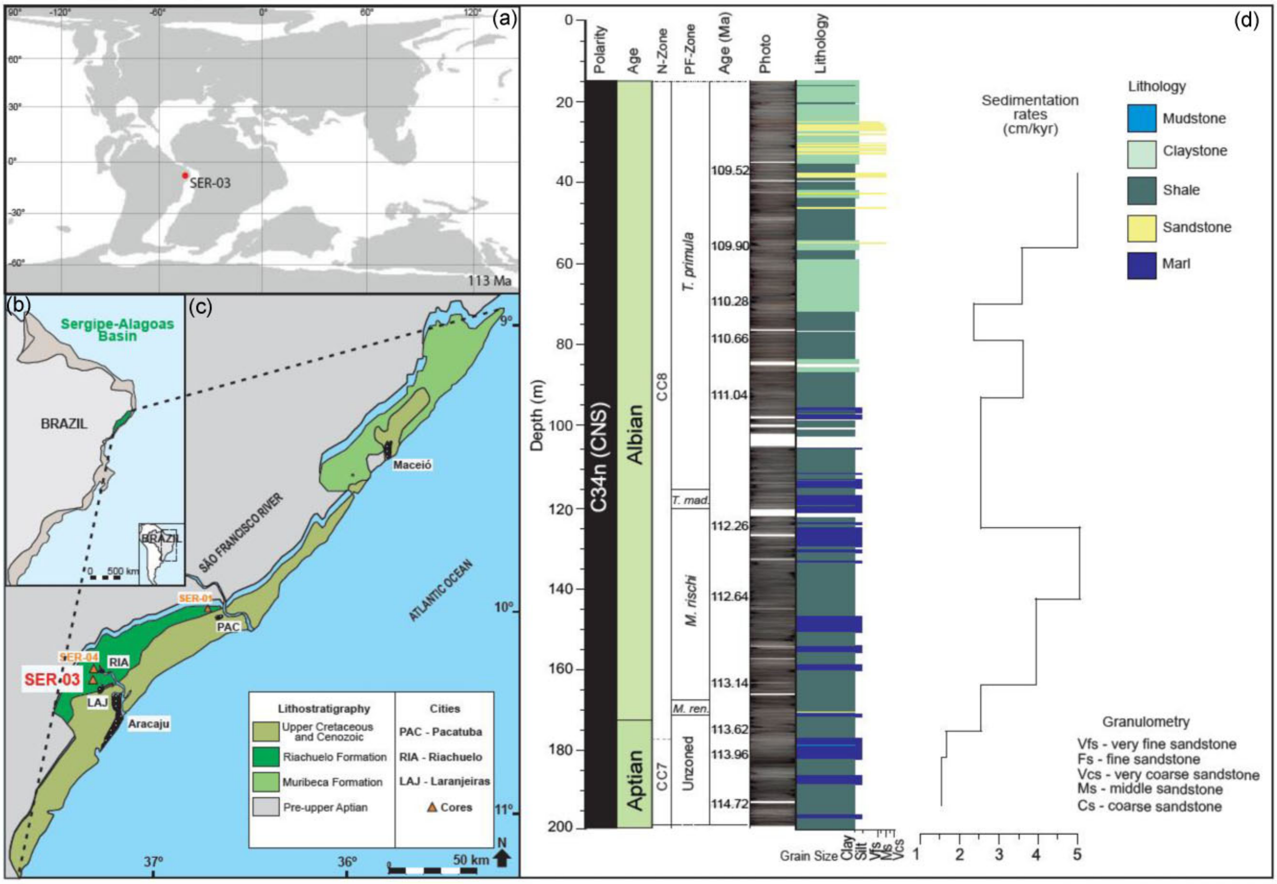

Figure 1. (a) Aptian–Albian paleogeographic reconstruction indicating the location of core SER-03 (red dot) ∼113 Ma. Paleogeographic map generated with the ODSN software available at http://www.odsn.de/odsn/services/paleomap/paleomap.html. (b) Present-day position of Sergipe-Alagoas Basin. (c) Present-day position of the SER-03 core in Sergipe-Alagoas Basin. (d) Paleomagnetic, biostratigraphic and sedimentological framework of core SER-03 (Fauth *et al.* 2021, 2022). Planktonic foraminiferal (PF-Zone), calcareous nannofossil (N-Zone) biozones, absolute ages and sedimentation rates are from Fauth *et al.* (2022).

In Fauth *et al.* (2021), two lithostratigraphic units were identified. Unit I spans the interval between 198 and 95.3 m and is primarily characterized by thick intercalated layers of dark grey shale and light grey marl. Within Unit I, two intervals exhibit dark grey shale at depths of 184.3–183.3 m and 153.0–151.5 m. Unit II is present in the interval between 95.3 and 5.8 m and consists mainly of thick intercalated layers of medium-light grey mudstone and medium-light grey shale (95.3–15.6 m), followed by light greyish-brown claystone (12.5–5.8 m). Additionally, fine- to medium-grained sandstones, forming millimetre- to centimetre-thick layers, are observed at specific depths ranging from 55.2 to 25.7 m.

3 AGE MODEL

The base of the Albian and, therefore, the Aptian–Albian boundary (∼113.0 Ma; Gradstein *et al.* 2020; Leandro *et al.* 2022) at core SER-03 is identified by the first occurrence of the planktonic foraminifera *Microhedbergella renilaevis* at 171.55 m (Fig. 1; Kennedy *et al.* 2017; Fauth *et al.* 2022; Leandro *et al.* 2022). Within the Albian, the first occurrence of *Ticinella primula* at 117.51 m was also considered a robust bioevent by Fauth *et al.* (2022). Planktonic foraminiferal, and calcareous nannofossil bioevents across the entire marine sedimentary succession were additionally constrained by astrochronology conducted by Fauth *et al.* (2022), which used 11 tie points to tune a 5 cm resolution natural gamma-ray series to the stable long eccentricity cycle (405 kyr) (Fig. 1d). This age model is integrated here with high-resolution paleomagnetic records spanning the interval between ∼114.7 and 109.5 Ma, falling within magnetochron C34n. The independently estimated ages for biostratigraphic markers align within one long eccentricity cycle with previous estimates (Gradstein *et al.* 2020), over a ∼5.2 Myr interval (Fauth *et al.* 2022).

4 MATERIALS AND METHODS

All measurements were conducted at the Laboratório de Paleomagnetismo e Geomagnetismo (USPMag) at the Universidade de São Paulo (USP). A total of 384 cubic samples (∼8 cm^3) were collected for paleomagnetic and rock magnetic analyses (mass normalized) from depths ranging from 15.88 to 198.47 m, approximately 183 m, excluding the top 15 m of the core, which consists of brown unconsolidated soil and weathered rock.

Initially, all samples were measured for magnetic susceptibility (χ) using the AGICO MFK1-FA multifunction Kappabridge (Dearing *et al.* 1996; Chadima & Hrouda 2007; Hrouda & Pokorný 2012) at two operating frequencies (low frequency, χ_{lf}, 976 Hz and high frequency, χ_{hf}, 15 616 Hz) in a magnetic field of 200 Am^{-1}.

Natural remanent magnetization (NRM) of all samples was stepwise AF demagnetized with peak fields up to 100 mT, at 17 field steps: NRM, 2, 4, 7, 10, 15, 20, 25, 30, 35, 40, 50, 60, 70, 80, 90 and 100 mT. Anhysteretic remanent magnetization (ARM) was induced using 100 mT in direct current, with a bias field of 0.05 mT, and subsequently demagnetized by applying the same AF treatment. The $\mathrm{ARM}_{100\mathrm{mT}}$ is used to infer the concentration of low-coercivity magnetic minerals (Kodama 2012).

Characteristic remanent magnetization (ChRM) directions were determined by interpreting vector end-point demagnetization diagrams (Zijderveld 1967). Magnetic components were calculated using principal component analysis (Kirschvink 1980). This method analyses the best-fitting straight line with maximum angular deviation (MAD) of $<15^\circ$. The analysis was conducted using the Remasoft 3.0 paleomagnetic software package (Chadima & Hrouda 2007). Since core SER-03 lacked azimuthal orientation, we relied on the inclination record to determine geomagnetic polarities.

Isothermal remanent magnetization (IRM) was measured by applying a field of 1 T (saturation isothermal remanent magnetization, SIRM, or $\mathrm{IRM}_{1000\mathrm{mT}}$) in a 2G Enterprises Pulse Magnetizer at USP-Mag, followed by a back field of 100 and 300 mT, and then subjected to AF demagnetization following the same afore mentioned steps. All AF demagnetization procedures for NRM, ARM and IRM remanences routines were conducted on 369 samples using a 2G Enterprises cryogenic magnetometer (model u-channel 755R) housed in a magnetically shielded room.

SIRM is used to identify down-core variations in the magnetic mineralogy of sediments in terms of relative amount of low-coercivity ferromagnetic minerals, that is magnetite, compared to high-coercivity antiferromagnetic minerals, that is hematite (Kodama 2012; Liu *et al.* 2012). Also, from the IRM data, the S-ratio ($\mathrm{S}_{300\mathrm{mT}} = [\mathrm{IRM}_{\text{-}300\mathrm{mT}}/\mathrm{IRM}_{1000\mathrm{mT}}]$) and 'hard' isothermal remanent magnetization ($\mathrm{HIRM} = [\mathrm{IRM}_{1000\mathrm{mT}} + \mathrm{IRM}_{\text{-}300\mathrm{mT}]}/2$) were calculated. These parameters indicate the relative concentration of low-versus high-coercivity minerals and reflect the magnetic signal from high-coercivity antiferromagnetic minerals (Thompson & Oldfield 1986; Kodama 2012; Liu *et al.* 2012). Regarding using the ratio $\mathrm{ARM}_{100\mathrm{mT}}$/SIRM, samples containing a large fraction of single domain (SD)-pseud-single domain (PSD) particles will have a higher ARM/SIRM ratio (Tauxe 1993; Kodama 2012). Finally, SIRM/χ_{lf}, is used for estimating grain-size variations (Tauxe 1993; Kodama 2012).

Hysteresis loops and back-field demagnetization were conducted to obtain parameters including saturation remanence (M_r), saturation magnetization (M_s), coercive force (H_c), and coercivity remanence (H_{cr}). The ratios of $M_\mathrm{r}/M_\mathrm{s}$ and $H_{\mathrm{cr}}/H_\mathrm{c}$ are useful in discriminating domain state and magnetic grain size (Day *et al.* 1977). These high-field measurements were executed using a variable field translation balance in a Vibrating Sample Magnetometer Micromag 3900 by Princeton–Lakeshore Cryotronics.

Magnetic susceptibility (χ) versus temperature (themormagnetic) curves were obtained using a Kappabridge KLY-4S coupled with a CS3 furnace (Chadima & Hrouda 2007), by heating and cooling from room temperature up to 700° C. ARM acquisition curves were analysed using the curve-fitting software MAX UnMix (e.g. Maxbauer *et al.* 2016). This method can determine mean coercivity (B_h), a dispersion parameter (DP), and a skewness factor (S). Additionally, $\mathrm{ARM}_{100\,\mathrm{mT}}$ values can be correlated with the concentration of SD and PSD or vortex grains (Roberts *et al.* 2017).

The relative paleointensity (RPI) variability was estimated by normalizing the NRM to susceptibility, ARM, and SIRM (e.g. Tauxe 1993; Lund *et al.* 2017). Although the results with χ, ARM and SIRM as normalizers produce almost identical patterns, we prefer to use ARM as the RPI proxy because it is more sensitive to the finest grains. Additionally, we applied the pseudo-Thellier method (Tauxe *et al.* 1995; Paterson *et al.* 2016), a non-heating paleointensity method used to explore magnetic field intensity variation recorded by thermally sensitive materials of both terrestrial and extraterrestrial origin. In this method, an alternating field is used to demagnetize the NRM's specimen and replace it with a laboratory-induced ARM (as an analogue of a thermoremanent magnetization). The pseudo-Thellier method serves as a normalization and has been widely used in sediment cores (Tauxe *et al.* 1995; de Groot *et al.* 2013; Paterson *et al.* 2016). However, some parameters were slightly relaxed from Paterson *et al.* (2016) due to the very rigorous metrics used in their criteria (Bono *et al.* 2019; Shcherbakova *et al.* 2020). All samples used in this work are approved by the following parameters of Paterson *et al.* (2016): MAD $\leq 10^\circ$, $n \geq 6$, $f \geq 0.45$, $\beta \leq 0.1$. The rest of the parameters related to the linear fit of the data (r^2, |k|, f_{resid}, α, and |bAA|) were relaxed because our values are close to the acceptable values reported by Shcherbakova *et al.* (2020). All data is reported in Appendix A1. Classical normalizations by χ, $\mathrm{ARM}_{15\mathrm{mT}}$ and $\mathrm{IRM}_{15\mathrm{mT}}$ were used to determine relative paleointensity curves and were compared to the curve resulting from the pseudo-Thellier method.

5 RESULTS

5.1 Magnetic mineralogy and grain size

χ_{lf} values ranged from 1.83×10^{-8} to $1.30 \times 10^{-7}\ \mathrm{m^3\,kg^{-1}}$, with a mean of $8.41 \times 10^{-8}\ \mathrm{m^3\,kg^{-1}}$. These values exhibited amplitude changes throughout the core. χ_{hf} varied between 1.27×10^{-7} and $1.82 \times 10^{-8}\ \mathrm{m^3\,kg^{-1}}$, with a mean of $8.18 \times 10^{-8}\ \mathrm{m^3\,kg^{-1}}$ (Fig. 2a), consistent with observations of χ_{lf}. The intensity of magnetization (NRM) ranged from 9.49×10^{-8} to $2.49 \times 10^{-9}\ \mathrm{Am^2\,kg^{-1}}$, with a mean of $2.68 \times 10^{-8}\ \mathrm{Am^2\,kg^{-1}}$ (Fig. 2b).

$\mathrm{ARM}_{100\mathrm{mT}}$ ranged from 3.31×10^{-8} to $2.82 \times 10^{-7}\ \mathrm{Am^2\,kg^{-1}}$, with a mean of $1.44 \times 10^{-7}\ \mathrm{Am^2\,kg^{-1}}$ (Fig. 2c). Intensity oscillations throughout the top half of the core exhibited more variability, while the middle and basal parts showed a well-marked negative peak at 113.70 Ma (177.08 m) and a positive peak at 113.9 Ma (180.15 m), with more regular behaviour. The SIRM behaviour resembled that of $\mathrm{ARM}_{100\mathrm{mT}}$ ranging from 8.81×10^{-7} to $1.37 \times 10^{-5}\ \mathrm{Am^2\,kg^{-1}}$, with a mean of $4.89 \times 10^{-6}\ \mathrm{Am^2\,kg^{-1}}$ (Fig. 2d). Although the negative and positive peaks in the older part had shorter amplitudes at 113.74 Ma (177.66 m) and 113.89 Ma (180.15 m), respectively, HIRM behaviour resembled that of SIRM, ranging from 7.97×10^{-7} to $1.16 \times 10^{-5}\ \mathrm{Am^2\,kg^{-1}}$ (Fig. 2e).

The S-Ratio remains remarkably constant, ranging from 0.34 to 1, with 85 per cent of the samples falling within the range of 0.79–0.89. Two peaks at a value of 1 are observed at 110.56 Ma (77.29 m) and 113.70 Ma (177.08 m) (Fig. 2f). The $\mathrm{ARM}_{100\,\mathrm{mT}}$/SIRM ratio ranged from 1.44×10^{-2} to 4.8×10^{-2}, with a mean of 3.16×10^{-2} (Fig. 2g). Oscillations follow along the core and increase in amplitude until approximately 112.0 Ma (around 118 m). Values continue to oscillate with a slight decrease in depth, but the oldest values never fall below 2.60×10^{-2} at 115.03 Ma (197.87 m)

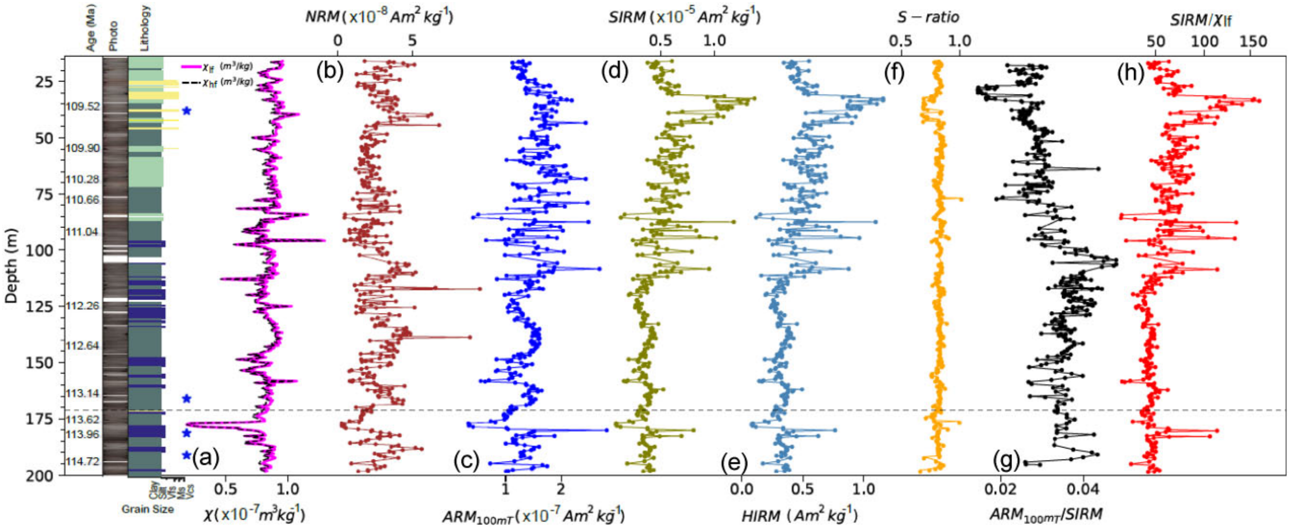

Figure 2. Trends depicted by rock magnetic proxies at core SER-03 over time. (a) Magnetic susceptibility (χ) in two different frequencies (χlf, 976 Hz and χhf, 15.616 Hz) in a field of 200 Am^{-1}. (b) Natural remanent magnetization. (c) Anhysteretic remanent magnetization induced at 100 (ARM100mT). (d) Saturation of isothermal remanent magnetization. (e) HIRM records changes in the concentration of magnetic minerals. (f) S-Ratio records relative changes in magnetite versus hematite. (g) ARM100mT/SIRM. (h) SIRM/χlf. Grey dashed line represents Aptian–Albian boundary reported in GTS 2020 (∼113.2 Ma; Gradstein *et al.* 2020); stars represent examples of samples subjected to stepwise AF demagnetization (190.05, 125.79, 76.38 and 23.75 m; see Fig. 6).

(Fig. 2g). The behaviour of the SIRM/χ_{lf} ratio is comparable to those of ARM$_{100\,\mathrm{mT}}$ and SIRM, ranging from 13.78 to 156.23 mA^{-1}, with a mean of 57.8 mA^{-1}. Two positive peaks are observed in the older interval at 113.9 Ma (180.15 m) and 114.04 Ma (182.64 m), respectively (Fig. 2h).

To obtain detailed magnetic mineralogy and grain-size information, we utilized χ-T curves, hysteresis loops, and IRM acquisition curves. χ-T curves indicate that magnetite and/or titanomagnetite are the dominant magnetic minerals, showing the most significant susceptibility decrease at approximately 580° C (Fig. 3). After heating, cooling curves plot above heating curves, consistent with mineral transformation during the heating process (e.g. Dunlop & Özdemir 1997; Muxworthy *et al.* 2023).

Hysteresis loops reveal the presence of low-coercivity minerals, which dominate magnetic properties of most samples (Fig. S1, Supporting Information). Additional magnetic mineralogical information was obtained using hysteresis loops (Table 1) for 13 representative samples. Hysteresis parameters (M_{r}, M_{s}, H_{cr} and H_{c}) and their ratios ($M_{\mathrm{r}}/M_{\mathrm{s}}$ and $H_{\mathrm{cr}}/H_{\mathrm{c}}$) (Table 1) can be utilized to characterize the domain structure (SD; PSD – or vortex; multidomain, MD) of magnetite in a Day plot (Day *et al.* 1977; Dunlop 2002a, b). Hysteresis ratios for representative samples exhibit consistent behaviour (Fig. 4), aligning with the mixing grain-size trend of magnetite between the SD and MD fields as defined by Dunlop (2002a, b).

IRM acquisition curves for representative samples were used to determine the magnetic mineralogy of the lithologies at room temperature (Fig. S2, Supporting Information). Saturating fields below 300 mT confirm the predominance of low-coercivity magnetic minerals such as magnetite and/or titanomagnetite. Unmixing coercivity distributions derived from ARM acquisition curves resulted in a two components model fit for all specimens (Figs 5a and b). Each component is characterized by its median coercive field (B_{h}) and dispersion parameter (DP; one standard deviation in log$_{10}$) (Maxbauer *et al.* 2016). A total of 31 samples were analysed along the studied interval (Table S1, Supporting Information).

The adjusted component (Figs 5a and b) is characterized by a B_{h} of 27–42 mT and a DP of 0.36–0.40. Following Egli (2004), this component is interpreted as detrital magnetite and/or eolian dust (Fig. 5c).

5.2 Paleomagnetic directions and RPI

The representative NRM demagnetization results of six samples from different depths are shown in Fig. 6. All demagnetized samples exhibit a well-defined single component toward the origin that can be isolated between 10 and 60 mT. We define this component as the ChRM, characterized by a MAD anchored to the origin of the Zijderveld diagram of less than 10°, the variations in the median destructive field (MDF, average field at which the initial intensity decays by 50 per cent (Fig. 7a), inclination (Fig. 7b), and MAD (Fig. 7c) of all samples throughout the SER-03 core time span.

RPI variability was estimated by normalizing NRM to susceptibility, ARM and SIRM (Figs 8a–c), as well as by employing the pseudo-Thellier method (Fig. 8d). Sediments from the core SER-03 are ideal for recovering relative paleointensity data due to their minimal variations in rock magnetic parameters throughout the record (less than a factor of 10, Fig. 2). We opted to use the 15 mT-step to quantify RPI estimates from NRM, ARM and SIRM, aiming to eliminate the viscous component of relatively low-magnetic stability as proposed by Levi & Banerjee (1976). The results of all normalized parameters produce nearly identical patterns across the entire record (Fig. 8). This resemblance between the results of normalized parameters and the pseudo-Thellier suggests that these determinations are robust and were not significantly affected by the viscous component (e.g. Tauxe 1993; Tauxe *et al.* 1995; de Groot *et al.* 2013; Paterson *et al.* 2016). In this method, the remaining NRM (NRM left) was plotted versus ARM gained, creating pseudo-Arai plots (Figs 9a–f). The slopes of the pseudo-Arai plots serve as a measure of relative paleointensity.

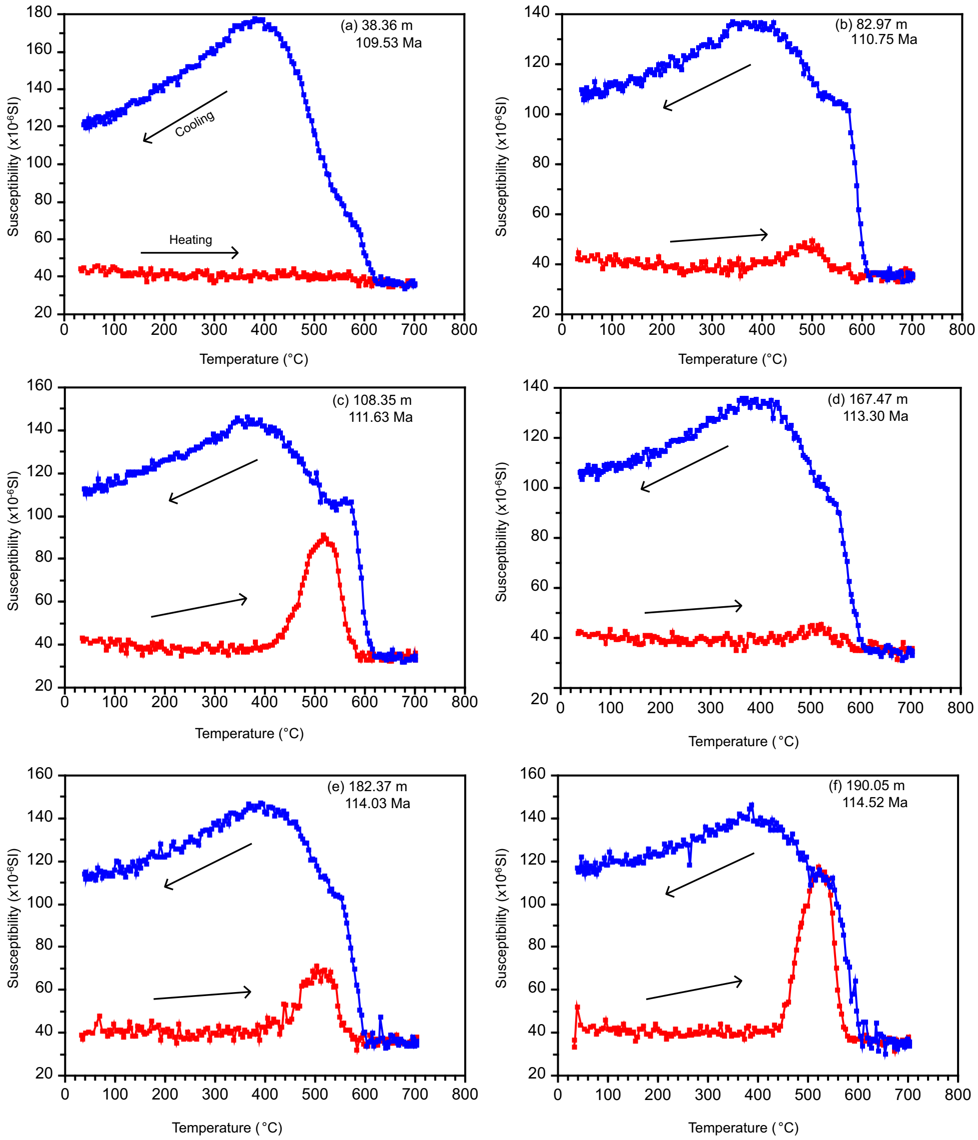

Figure 3. Temperature dependence of magnetic susceptibility curves for six representative samples from core SER-03. Heating and cooling segments are indicated by red and blue curves or pointing right and left arrows, respectively.

6 DISCUSSION

6.1 Magnetic mineralogy and grain size

During and after sediment accumulation, environmental factors can influence the magnetic properties of sediments (Tauxe 1993). To obtain reliable directional palaeomagnetic secular variation (PSV) and relative paleointensity estimates, it is important to investigate whether the NRM and RPI records exhibit a relationship with environmental parameters and magnetic mineralogy. The NRM of sedimentary rocks is acquired at the time of sediment deposition, however it is necessary to remove secondary overprints that were acquired at later times.

Rock magnetic data for core SER-03 highlights the predominance of magnetite with a Curie temperature of 580° C as the main carrier of magnetization in these sediments. A change in the slope of heating curves between 420 and 580° C indicates the additional presence of titanomagnetite (Fig. 3) (e.g. Muxworthy *et al.* 2023). Stepwise acquisition of IRM in fields up to 1 T documents that more than 90 per cent of SIRMs were saturated in a field of 300 mT (Fig. S2, Supporting Information), suggesting that low-coercive magnetic mineral, such as magnetite and/or titanomagnetite, are predominant within the sediments. $ARM_{100\,mT}$ data and low values of SIRM support the presence of low-coercivity minerals, such as magnetite (Figs 2c and d) (e.g. Kodama 2012; Liu *et al.* 2012). The S-ratio varies from 0.79 to 0.89 for most samples, also indicating magnetite and/or titanomagnetite as the dominant magnetic mineral (King *et al.* 1982; Thompson & Oldfield 1986). The S-ratio and HIRM (Bloemendal *et al.* 1992; Liu *et al.* 2007) allows inferring relative concentrations of hard and soft magnetic minerals within the examined interval. Between 109.5 and 114.7 Ma, in ∼85 per cent of the samples, these values suggest a predominance of low-coercivity magnetic minerals throughout the ∼5.2 Myr interval. The remaining samples display an increased abundance of high-coercivity magnetic minerals, namely due to the presence of

Table 1. Measured hysteresis parameters and their ratios for selected sediments samples from the SER-03.

Sample	*Depth(m)*	*Age (Ma)*	*Mrs* ($Am^2\ kg^{-1}$)	*Ms* ($Am^2\ kg^{-1}$)	*Mrs/Ms*	*Hcr (mT)*	*Hc (mT)*	*Hcr/Hc*
SER03_023_25	23.25	109.23	5.70×10^{-5}	2.70×10^{-4}	2.11×10^{-1}	3.60×10^{-2}	1.09×10^{-2}	3.31
SER03_038_36	38.36	109.53	8.03×10^{-5}	8.32×10^{-4}	9.66×10^{-2}	3.80×10^{-2}	9.79×10^{-3}	3.88
SER03_040_97	40.07	109.58	9.58×10^{-5}	9.13×10^{-4}	1.05×10^{-1}	4.65×10^{-2}	1.07×10^{-2}	4.33
SER03_043_85	43.85	109.64	3.06×10^{-8}	3.43×10^{-7}	8.91×10^{-2}	3.65×10^{-2}	7.57×10^{-3}	4.82
SER03_044_35	44.85	109.65	7.73×10^{-5}	6.65×10^{-4}	1.16×10^{-1}	4.55×10^{-2}	1.06×10^{-2}	4.31
SER03_063_40	63.40	110.08	4.81×10^{-5}	3.32×10^{-4}	1.45×10^{-1}	4.17×10^{-2}	1.02×10^{-2}	4.11
SER03_077_85	77.85	110.59	3.55×10^{-5}	3.58×10^{-4}	9.92×10^{-2}	3.74×10^{-2}	9.64×10^{-3}	3.88
SER03_080_50	80.50	110.69	6.11×10^{-5}	5.43×10^{-4}	1.13×10^{-1}	3.52×10^{-2}	1.07×10^{-2}	3.29
SER03_128_99	128.99	112.35	3.11×10^{-5}	5.56×10^{-4}	5.60×10^{-2}	3.56×10^{-2}	7.87×10^{-3}	4.52
SER03_145_09	145.09	112.67	4.26×10^{-5}	5.31×10^{-4}	8.01×10^{-2}	2.45×10^{-2}	8.93×10^{-3}	2.74
SER03_154_51	154.51	112.91	3.52×10^{-5}	1.42×10^{-4}	2.48×10^{-1}	3.61×10^{-2}	2.60×10^{-2}	1.39
SER03_167_47	167.47	113.30	4.19×10^{-5}	3.42×10^{-4}	1.23×10^{-1}	3.29×10^{-2}	1.24×10^{-2}	2.66
SER03_182_37	182.37	114.03	2.83×10^{-5}	4.28×10^{-4}	6.63×10^{-2}	3.86×10^{-2}	8.22×10^{-3}	4.69

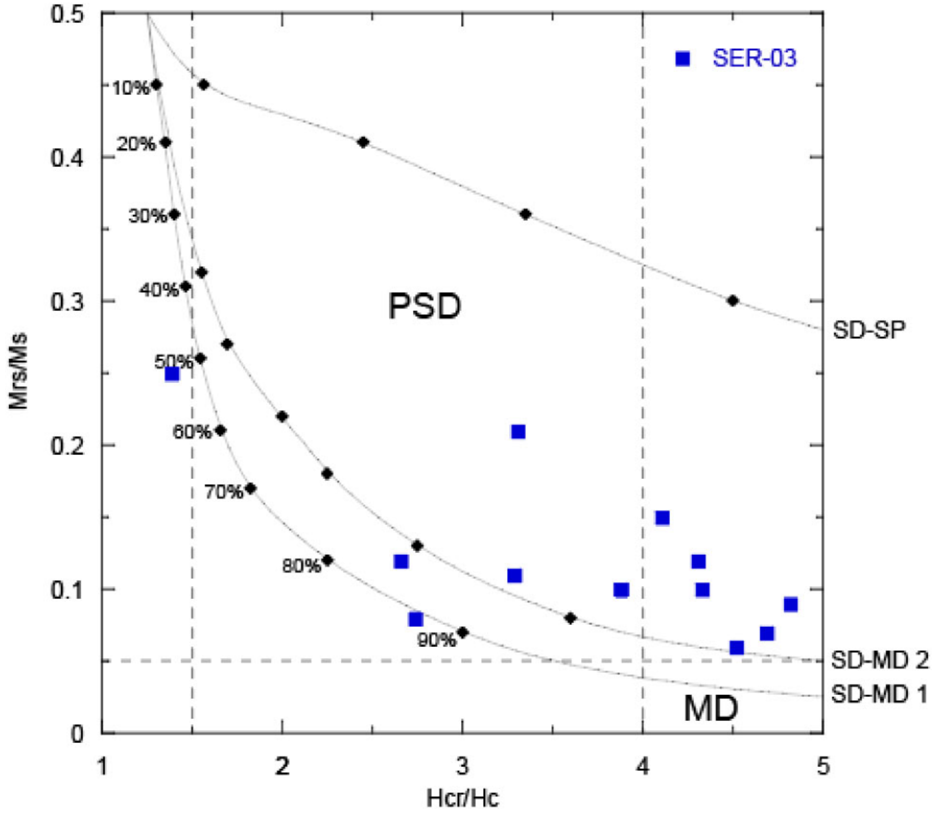

Figure 4. Day plot (Day *et al.* 1977) for representative samples from core SER-03. The domains represented in the M_{rs}/M_s versus H_{cr}/H_c diagram are indicative of PSD or vortex state, and multidomain (MD) magnetic particles. Theoretical mixing curves 1 and 2 are those expected for admixtures of MD, single domain (SD), and superparamagnetic (SP) magnetite for different median sizes of MD grains (Dunlop 2002a, b). Percentages along these curves refer to the volume fraction of SP or MD grains.

hematite and/or goethite, as indicated by the associated S-ratio minima (Figs 2e and f). The presence of detrital magnetite and/or aeolian dust is also inferred from unmixing coercivity distributions derived from ARM acquisition curves. ARM acquisition curves, according to Egli (2004), suggest that these components can be interpreted as related to detrital magnetite and/or aeolian dust input (Maxbauer *et al.* 2016) (Fig. 5c).

Compared to theoretical hysteresis trends for mixtures of hyperfine SP, SD and coarse MD grains (Dunlop 2002a, b) on a Day plot (Day *et al.* 1977), the measured data from core SER-03 generally align parallel to the SD–MD mixing curve (Fig. 4). Magnetic concentration parameters (χ, ARM$_{100mT}$, HIRM and SIRM), indicate slight variations but remain within one order of magnitude (Fig. 2), suggesting that magnetic concentration in the core is moderately homogeneous with respect to depth.

ARM$_{100mT}$/SIRM and ARM/χ_{lf}, typically used to estimate grain-size variations of magnetic particles (Yamazaki & Oda 2005; Yamamoto *et al.* 2007; Yamazaki *et al.* 2008), exhibit variations similar to those of concentration parameters, and remained within one order of magnitude. Samples containing a high fraction of SD-PSD particles are characterized by a higher ARM$_{100\,mT}$/SIRM ratio (Kodama 2012), particularly in the bottom half of the SER-03 core and around 111 Ma (Fig. 2f). The SIRM/χ_{lf} ratio is used to assess grain-size variations of magnetic minerals present in

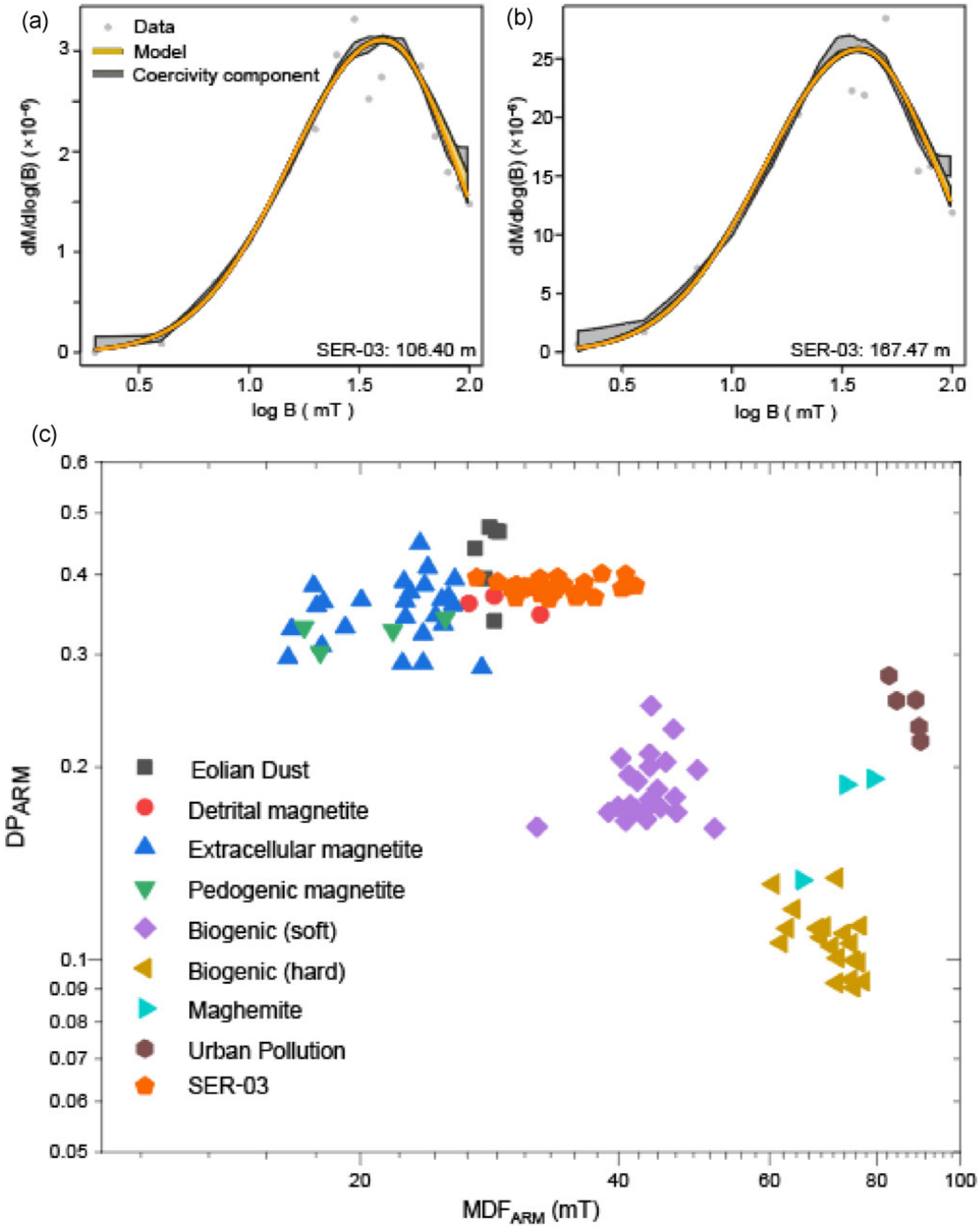

Figure 5. (a) and (b) Examples of coercivity analysis using the MAX Unmix web application (Maxbauer *et al.* 2016). (c) ARM parameters (DP: dispersion parameter and MDF: median destructive field) for magnetite and maghemite in different environments (Egli 2004).

the sample and is preferred over the ARM/χ_{lf} ratio because the latter is strongly dependent on the concentration of magnetic particles in a sample (Tauxe 1993). Grain size can significantly influence magnetic properties of a material. The SIRM/χ_{lf} ratio at core SER-03 showed higher values around 109.5, 111.0–112.0, and 114.0 Ma. Higher values may indicate smaller grain sizes of magnetic particles, whereas lower ratios may indicate larger grain sizes (Fig. 2g).

6.2 PSV records and short reversals

Continuous directional paleomagnetic data for the CNS are scarce in the South Hemisphere (e.g. Doubrovine *et al.* 2019), hampering the use of Earth's magnetic field short variations (from secular and millennial-scale variations) as correlation and dating tools (Korte *et al.* 2019). Here, for the first time, we present a continuous record of the Earth's magnetic field variations from 114.5 to 109.5 Ma (Fauth *et al.* 2022), from core SER-03, Sergipe–Alagoas Basin. Rock magnetic data suggest that the obtained ChRMs are of detrital origin and are most likely related to primary magnetizations, allowing the study of the Earth's magnetic field variation during the CNS (e.g. Satolli *et al.* 2008). Fossils and geochemical data also reveal primary signals, particularly reflecting the moderate to good preservation of calcareous nannofossil assemblages (Fauth *et al.* 2022; Luft-Souza *et al.* 2022). The geochemical records spanning OAE1b show trends similar to those reported for North Atlantic and Tethyan sections (Fauth *et al.* 2022). In addition, several precautions were taken during drilling activities (Fauth *et al.* 2021).

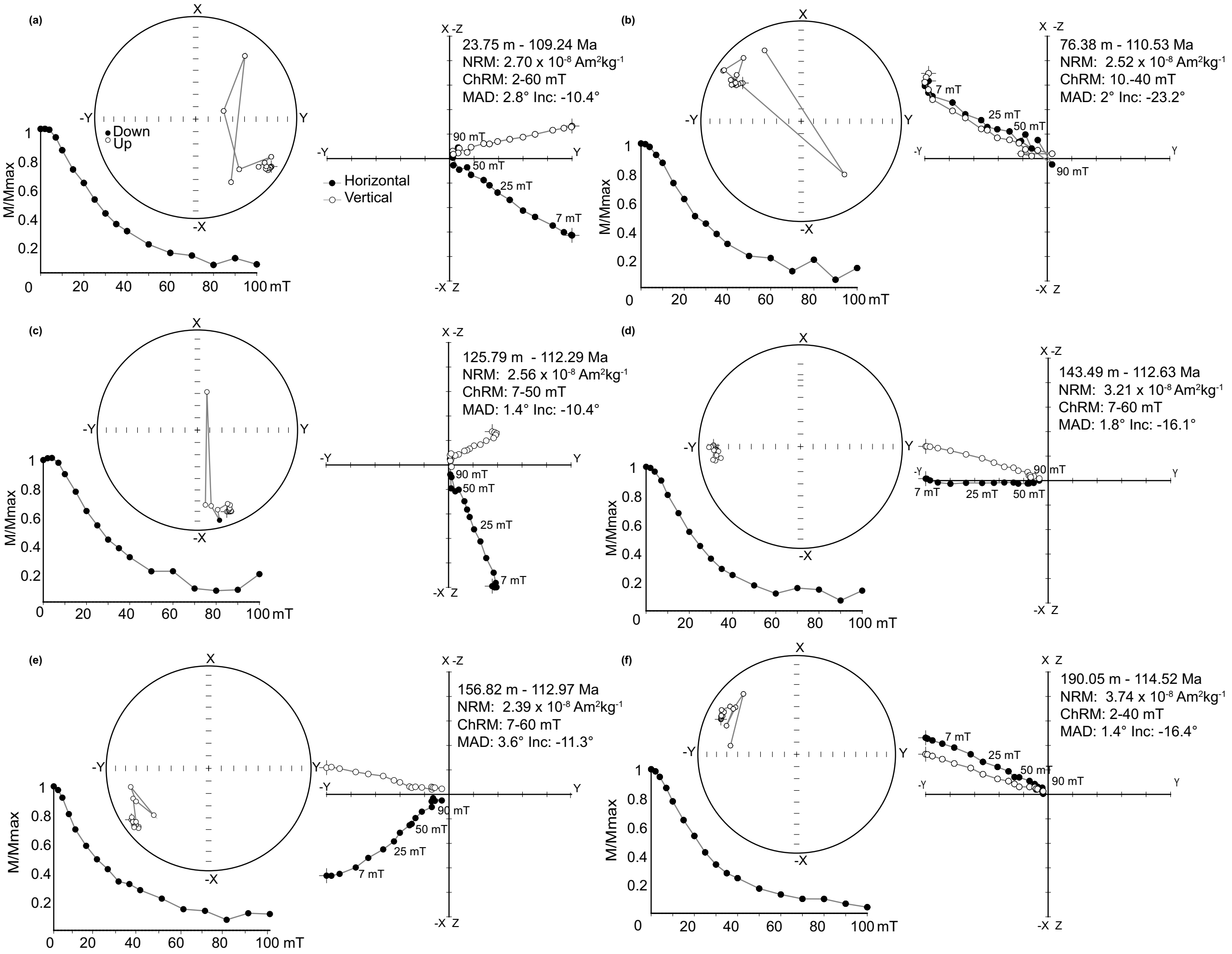

Figure 6. Alternating field demagnetization diagrams for selected samples from SER-03 presented as stereographic projection, Zijderveld plots (Zijderveld 1967; Kirschvink 1980), and normalized magnetization versus field plots. In the Zijderveld plots solid symbols represent declination, while open symbols represent inclination. In the stereonets, solid symbols indicate normal components, and open symbols indicate reverse components. NRM refers to natural remanent magnetization, MAD indicates maximum angular deviation, and ChRM denotates characteristic remanent magnetization.

The paleomagnetic record from core SER-03 exhibits mostly negative inclinations, within a mean value of approximately –16.3°, indicating deposition during CNS, and in agreement with biostratigraphic framework and the astronomically calibrated age model in Fauth *et al.* (2022). Similar results have been reported in the same region and time interval for volcanic rocks (e.g. Font *et al.* 2009). However, eight samples in the studied record show positive inclinations, suggesting short periods of reversed field (Fig. 7). There are a few reports of short reversal events within the CNS (e.g. Vandenberg *et al.* 1978; Tarduno 1990; Gilder *et al.* 2003; Font *et al.* 2009; He *et al.* 2012; Zhang *et al.* 2021). Zhang *et al.* (2021), and Yoshimura (2022) provide a summary of studied reversals in marine and terrestrial sediments and volcanic rocks. Notably, some events have been reported near the Aptian–Albian boundary at approximately 113.3 ± 1.6 Ma (Gilder *et al.* 2003). In the SER-03 record, three consecutive samples with positive inclinations occur at 92.91, 93.51 and 94.57 m, corresponding to 111.03, 111.05 and 111.09 Ma (spanning ~60 kyr), respectively. However, additional high-resolution data are needed to confirm such short-lasting polarity events.

Inclination values from core SER-03 core are consistent between consecutive samples and reveal gradually varying directional changes (Fig. 7). Notably, these changes are unrelated to variations of lithology or rock magnetic properties (Fig. 2). According to the paleogeographic reconstruction by Torsvik (2012), the mean paleomagnetic inclination of −16.3° indicates that the core site was located at approximately 8° south during the Cretaceous (~110 Ma). This consistency also supports the conclusion that the ChRM has not been altered since its acquisition, and there is no evidence of inclination flattening in the sediments.

The new paleomagnetic record from core SER-03 core is based on a total of 384 samples distributed over the ~5.2 Myr interval. Based on sedimentation rates calculated by astronomically calibrated age model of core SER-03 (Fig. 1), we present the mean temporal resolutions between 9.2 and 30.4 ka (Table S2, Supporting Information). The short-term millennial-scale variations reconstructed for this period are different than those observed in higher reversal rates periods (McFadden *et al.* 1991), it is a stable normal polarity period. Due to the scarcity of PSV data, the reversal curves are still a motive of debate in the literature (McFadden *et al.* 1991; Tarduno *et al.* 2002;

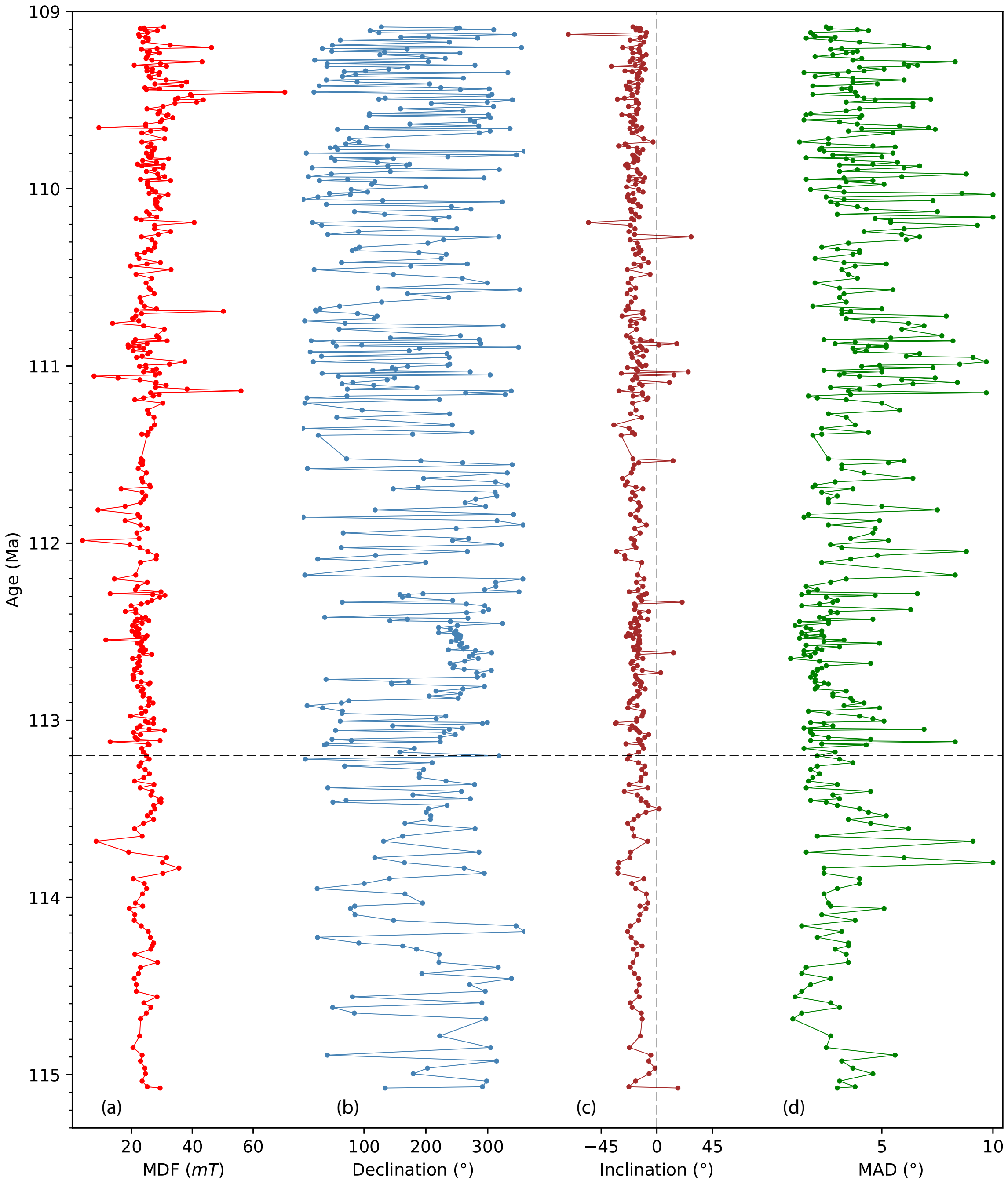

Figure 7. Variation of (a) MDF, (b) declination, (c) inclination and (d) MAD along age at core SER-03. Horizontal dashed line represents the Aptian–Albian boundary reported in GTS 2020 (∼113.2 Ma; Gradstein *et al.* 2020).

Biggin *et al.* 2008; Doubrovine *et al.* 2019). Brief reversed-polarity chrons have been documented during the CNS (Larson & Chase 1972; Keating & Helsley 1978; Ryan *et al.* 1978; Tarduno 1990; Shi *et al.* 2004; Zhang *et al.* 2021). Ramos *et al.* (2024) indicates an age of 117.03 ± 0.14 Ma for ISEA and 116.17 ± 0.14 Ma for reversal ‘2’ with timespans of ∼20 and ∼10 kyr, respectively.

The short duration of these reversals contributes to the difficulty in detecting them, which is highly dependent on sampling rates and the limitations of deep-tow surveys. Numerical model simulations suggest that the geodynamo operated at peak efficiency with a unique heat flux condition at the core–mantle boundary (CMB) during the CNS (Glatzmaier & Roberts 1995; Tarduno *et al.* 2001, 2002; Glatzmaier 2002; Coe & Glatzmaier 2006; Kageyama *et al.* 2008; Lhuillier & Gilder 2013; Aubert & Finlay 2019). Nevertheless, Amit & Olson (2015) estimated a decrease in CMB heat flux of about 30 per cent relative to the present day for both the CNS and the Kiaman Reverse Polarity Superchron. They also suggest that intervals with higher reversal frequencies during Jurassic times should be associated with core heat flux levels equal to or higher than those of the present day. Furthermore, assessments of the relative contribution of the b/a ratio—antisymmetric/symmetric harmonic terms (Franco *et al.* 2019)—which enables tracking the

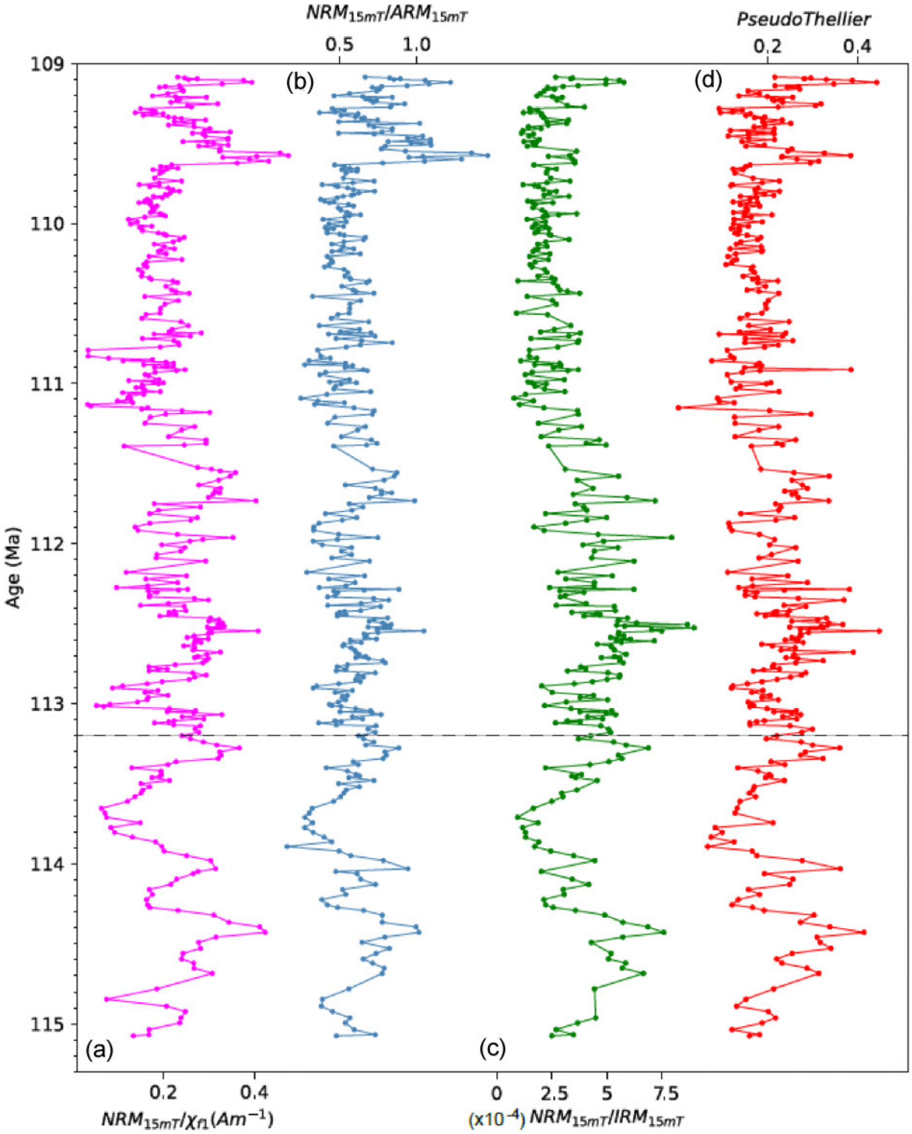

Figure 8. Normalized estimates of RPI: (a) NRM_{15mT}/χ, (b) NRM_{15mT}/ARM_{15mT}, (c) NRM_{15mT}/IRM_{15mT} and (d) curve of pseudo-Thellier versus age. Grey dashed line represents the Aptian–Albian boundary reported in GTS 2020 (∼113.2 Ma; Gradstein *et al.* 2020).

time evolution of the relative contributions of dipole and non-dipole fields and can be considered a predictor of reversal frequency (Coe & Glatzmaier 2006), indicate a decreasing trend in the b/a ratio (reflecting an enhancement of the symmetric, non-dipole harmonic terms) from the onset of the CNS to ∼110 Ma. This trend is inversely proportional to the CMB heat flux and favours an increase in the geomagnetic reversal rate during this interval. Our data thus are an important contribution to CNS geomagnetic modelling efforts, as they add new paleomagnetic direction contraints to the South American database.

6.3 RPI records

With deposition rates between 1.5 and 5.0 cm kyr^{-1} between 114.7 and 109.5 Ma (Fauth *et al.* 2022), core SER-03 provides high-resolution geomagnetic field data across the Aptian–Albian transition, providing a record of paleosecular variation during the CNS. The paleomagnetic signal is carried mainly by magnetite and the magnetic concentration is mostly constant throughout the ∼5.2 Myr interval, therefore the core SER-03 constitutes an opportunity to examine not only directional changes, but also the distribution of relative paleointensities. In fact, all criteria for assessing the reliability of the relative paleointensity data (King *et al.* 1983; Tauxe 1993; Paterson *et al.* 2016) are satisfied for core SER-03.

RPI during the Aptian shows variations consistent with the few available absolute paleointensity records (Fig. 10). Virtual dipole moments in the CNS have been reported as ranging from 1.1 to 19.9×10^{22} Am^2 (Fig. 10). The reported time-averaged dipole moments vary from different studies (e.g. Yamamoto & Tsunakawa 2005; Tsunakawa *et al.* 2009; Tauxe *et al.* 2013; Yamazaki & Yamamoto 2014; Ahn *et al.* 2016; Kato *et al.* 2018; Bono *et al.* 2019; Yoshimura *et al.* 2020). We choose to compare our data with absolute paleointensity data due to the lack of relative paleointensity records for the CNS.

Cronin *et al.* (2001) proposes a curve of relative palointensity based on sediments from the Umbria-Marche Basin, but their record is expressed only in stratigraphic units, not in absolute time,

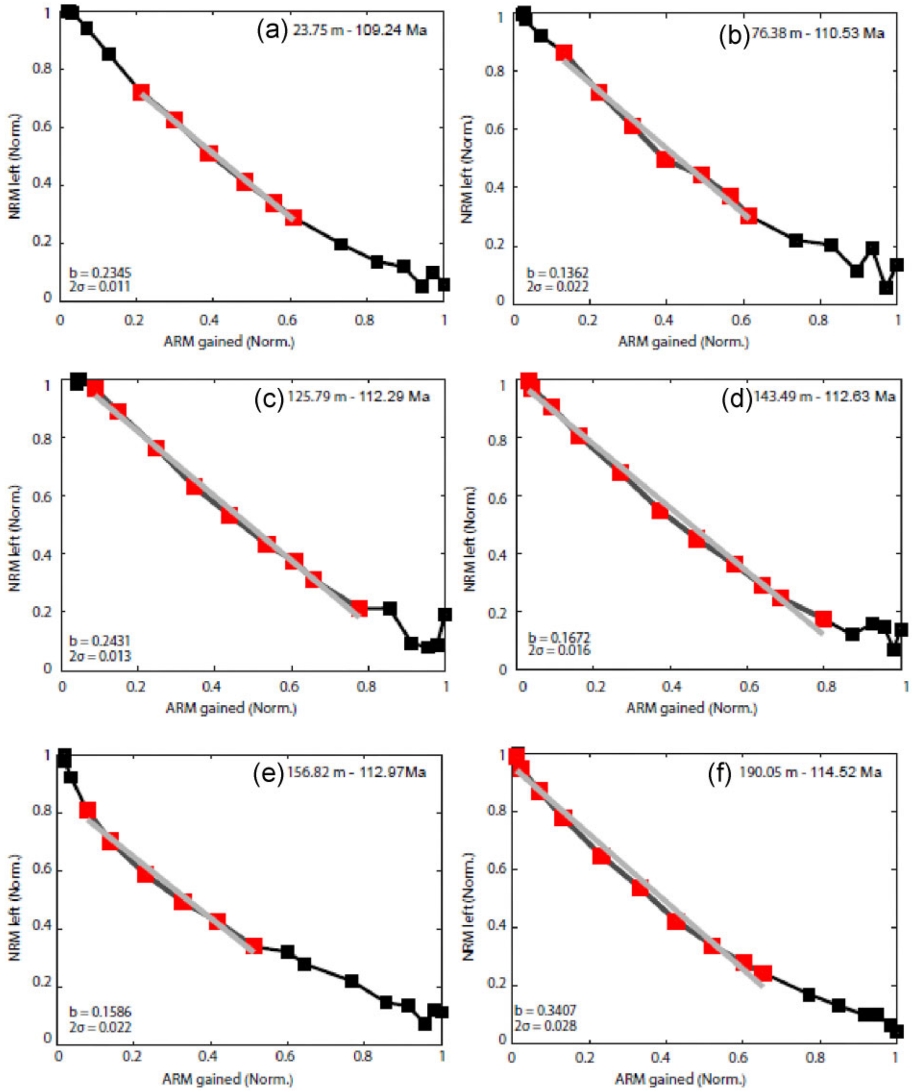

Figure 9. (a)–(f) Pseudo-Arai plots of representative samples. The slopes (b) of the straight lines represent relative paleointensities, and the uncertainty in the slopes is 2σ.

hampering the correlation with our section. Furthermore, Cronin *et al.* (2001) worked on a sedimentary section date as 89.5 to 85 Ma, spanning a different time interval than the core SER-03 record. However, we compare our data with Granot *et al.* (2012) during the same interval of the CNS (Granot *et al.* 2012). The magnitude of variations and their wavelength is similar in both records (Fig. 10). However, some disagreements can be related to the difference resolution of our data (9.2–30.4 kyr) and the deep-tow anomaly (∼0.1 and 2.3 Myr) of Granot *et al.* (2012). Based on a spectral analysis, our data shows that the more important variation are >100 kyr. Our analysis highlights the periodicities which contribute most to the signal have periods greater than 1 Myr.

We also compared the relative paleointensity record from this study with absolute paleointensity data. We observe periods of high- and low-intensity field (Tauxe & Hartl 1997; Constable *et al.* 1998), with high (114.8–114.2 Ma) and low (114.2–113.5 Ma) values at core SER-03 (Fig. 10). Our data show a quasi-cyclic paleointensity variations, consistent with temporal amplitude changes of marine magnetic anomalies during the CNS (Granot *et al.* 2012). Our new RPI data show that the geomagnetic field changed in both intensity and direction, and it was not completely stable during the studied time interval of the CNS. These results are in agreement with previously published data that suggest both intensity and directional variations during the CNS (e.g. Lhuillier *et al.* 2016; Doubrovine *et al.* 2019; Dembo *et al.* 2022; Liu *et al.* 2024).

Overall, the frequency of short (millennial) geomagnetic instabilities recognized during the CNS remains substantially lower when compared to other time intervals (e.g. Gradstein *et al.* 2020). The recognition of geomagnetic instabilities of short duration can serve as a tool for dating and correlating sections deposited in periods where the field is remarkably stable, and the lack of reversals hampers the use of magnetostratigraphy as a dating tool. Changes in intensity and inclinations within CNS indicate that geodynamo is much more dynamic than previously estimated. Numerical models of the geodynamo suggest that during superchrons, the geomagnetic field exhibits reduced variability and higher dipole moments compared to periods of frequent polarity reversals (Olson *et al.* 2010;

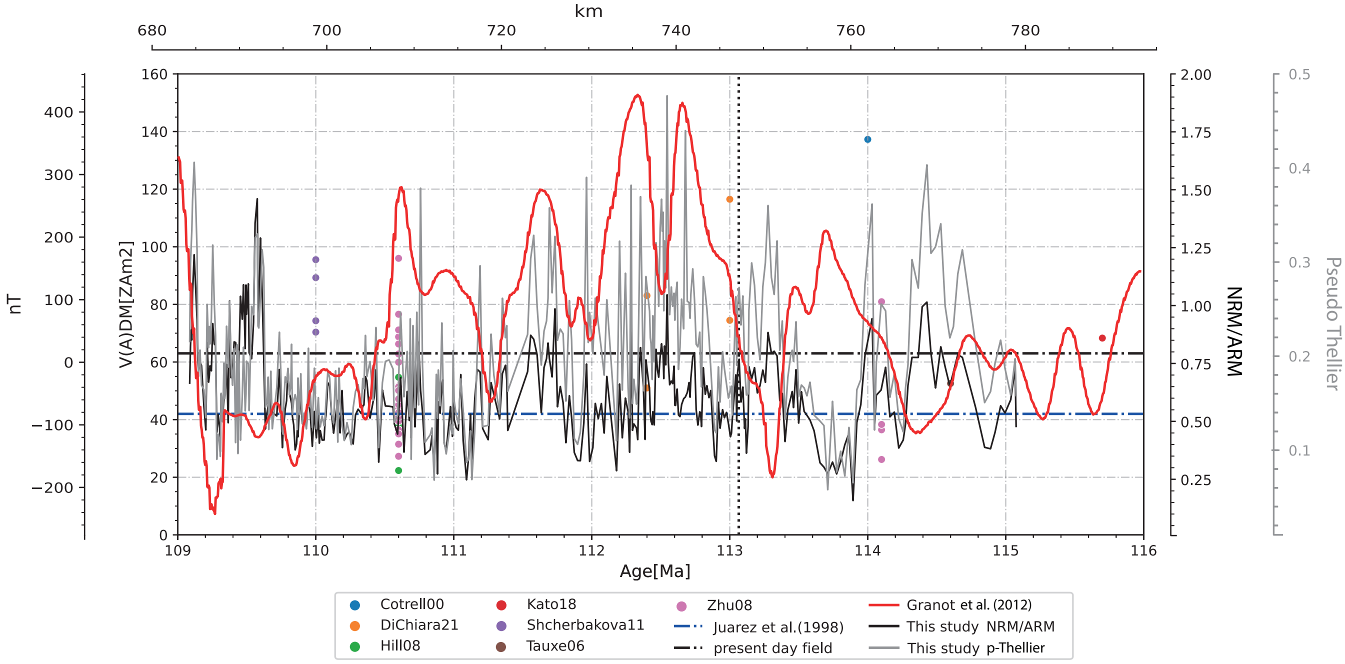

Figure 10. Relative paleointensity (NRM_{15mT}/ARM_{15mT} and Pseudo-Thellier) and virtual dipole moment (V(A)DM in ZAm^2) versus age (Ma) for the studied interval during the CNS, red curve represents Granot *et al.* (2012) data, dashed blue and grey lines represent the average field intensity from Juarez *et al.* (1998) and the present-day field (Cottrell & Tarduno 2000; Tauxe 2006; Hill *et al.* 2008; Zhu *et al.* 2008; Shcherbakova *et al.* 2011; Kato *et al.* 2018; Di Chiara *et al.* 2021). Vertical dashed line represents the Aptian–Albian boundary reported in the GPTS 2020 (∼113.2 Ma; Gradstein *et al.* 2020).

Driscoll & Olson 2011), which is related with the distribution of the heat flux along the CMB. However, these models assume uniform properties of the field within each polarity interval, which is not always confirmed by data (Larson & Olson 1991; Olson *et al.* 2010; Amit & Olson 2015; Hounslow *et al.* 2018; Franco *et al.* 2019). The age, frequency and observations remain poorly constrained due to a lack of paleomagnetic sampling and precise chronological control. Our new data will contribute to future runs numerical simulations of the geodynamo to better understand the variability of intensity and direction of the Earth's magnetic field during the CNS.

7 CONCLUSIONS

In this study, a comprehensive magnetostratigraphic analysis of core SER-03, Sergipe–Alagoas Basin, unveiled an extended normal polarity interval associated with the CNS, punctuated by sporadic short-lived reversed polarities. This offers a fresh perspective for correlating and calibrating RPI records within this timeframe. The following conclusions were drawn:

(1) Rock magnetic analyses indicated primary magnetizations for the entire interval with detrital magnetite as primary component, predominantly characterized by PSD and low coercivity. The χ, ARM and SIRM data suggest moderate concentration variations, thus fulfilling the commonly accepted criteria for establishing RPI records.
(2) Our data show short periods of reversed field within the studied interval of the CNS, suggesting higher magnitude of PSV variability than previously thought.
(3) RPI curves were obtained using both the $NRM_{15\,mT}/ARM_{15\,mT}$ and pseudo-Thellier records from 114.7 and 109.5 Ma. These curves show a quasi-cyclic behaviour during the studied interval of the CNS.
(4) The reconstructed RPI records showed long-term variations (∼1 Ma) throughout the CNS, thus suggesting that these RPI records predominantly reflected the behaviour of the global dipolar contribution of the geomagnetic field.

Our data indicate that the geomagnetic field and geodynamo during the CNS were dynamic. This finding underscores the utility of RPI data for elucidating the behaviour of the Earth's magnetic field during extended periods of polarity stability such as the CNS.

ACKNOWLEDGMENTS

This work has been (partially) performed at USPMag lab at Instituto de Astronomia, Geofísica e Ciências Atmosféricas (IAG) at Universidade de São Paulo (USP) funded by PETROBRAS. The authors thank PETROBRAS for financial support within the Magnetoestratigrafia project and Aptian–Albian Integrated Biostratigraphy in the Sergipe–Alagoas Basin (BIOSEAL) project. We thank the technical staff at the Technological Institute for Paleoceanography and Climate Changes (itt OCEANEON—UNISINOS University) for assistance with SER-03 core acquirement and biostratigraphic analyses; we acknowledge the Fundação de Amparo à Pesquisa do Estado do Rio Grande do Sul (FAPERGS) for financial support. We also thank 'National Council for Scientific and Technological Development—CNPq for the sandwich scholarship to the Istituto Nazionale di Geofisica e Vulcanologia, (grant 200824/2022–8) to RGM. and the research fellowship (grant 307309/2023–1) to KGDK. The authors appreciate

Professor Roi Granot and anonymous reviewers for their suggestions and useful comments, and the editorial work of Professor Andrew Biggin. We thank Prof. Daniel Ribeiro Franco for the discussions.

SUPPORTING INFORMATION

Supplementary data are available at *GJIRAS* online.

Figure S1. Hysteresis loops after paramagnetic correction of representative samples from core SER-03.
Figure S2. IRM acquisition curves of representative samples from core SER-03.
Table S1. ARM UnMix parameters of 31 samples. Depth, mean coercivity (B_h) and DP are shown.
Table S2. Temporal resolution, time interval in Ma and their respective sedimentation rates, number of analysed samples, and the mean sampling rate (years) per sample in each interval. See Fig. 1 for the sedimentation rates for each interval.

DATA AVAILABILITY

The data underlying this article are available in the article and in its online supplementary material.

REFERENCES

Ahn, H.-S., Kidane, T., Yamamoto, Y. & Otofuji, Y.-I., 2016. Low geomagnetic field intensity in the Matuyama Chron: palaeomagnetic study of a lava sequence from Afar depression, East Africa, *Geophys. J. Int.,* **204**(1), 127–146.

Amit, H. & Olson, P., 2015. Lower mantle superplume growth excites geomagnetic reversals, *Earth Planet. Sci. Lett.,* **414,** 68–76.

Aubert, J. & Finlay, C.C., 2019. Geomagnetic jerks and rapid hydromagnetic waves focusing at earth's core surface, *Nat. Geosci.,* **12,** 393–398.

Aubert, J., Tarduno, J.A. & Johnson, C.L., 2010. Observations and models of the long-term evolution of Earth's magnetic field, *Space Sci. Rev.,* **155,** 337–370.

Bengtson, P., 1983. The Cenomanian-Coniacian of the Sergipe Basin, Brazil, *Fossils Strata,* **12,** 1–78.

Bengtson, P., Zucon, M.H. & Sobral, A.C.S., 2018. Cretaceous ammonite zonation of the Sergipe Basin, northeastern Brazil, *Cretac. Res.,* **88,** 111–122.

Biggin, A., Piispa, E., Pesonen, L., Holme, R., Paterson, G.A., Veikkolainen, T. & Tauxe, L., 2015. Palaeomagnetic field intensity variations suggest mesoproterozoic inner-core nucleation, *Nature,* **526,** 245–248.

Biggin, A., Steinberger, B., Aubert, J., Suttie, N., Holme, R., Torsvik, T.H., van der Meer, D.G. & van Hinsbergen, D., 2012. Possible links between long-term geomagnetic variations and whole-mantle convection processes, *Nat. Geosci.,* **5,** 526–533.

Biggin, A.J., Van Hinsbergen, D.J., Langereis, C.G., Straathof, G.B. & Deenen, M.H.L., 2008. Geomagnetic secular variation in the cretaceous Normal Superchron and in the Jurassic, *Phys. Earth Planet. Inter.,* **169**(1), 3–19.

Bloemendal, J., King, J.W., Hall, F.R. & Doh, S.-J., 1992. Rock magnetism of late neogene and pleistocene deep-sea sediments: relationship to sediment source, diagenetic processes, and sediment lithology, *J. Geophys. Res.,* **97,** 4361–4375.

Bono, R.K., Tarduno, J.A., Nimmo, F. & Cottrell, R.D., 2019. Young inner core inferred from Ediacaran ultra-low geomagnetic field intensity, *Nat. Geosci.,* **12,** 143–147.

Brown, M.C. *et al.*, 2015a. GEOMAGIA50.V3: 2. A new paleomagnetic database for lake and marine sediments, *Earth Planets Space,* **67,** 70, doi:10.1186/s40623-015-0233-z.

Brown, M.C., Donadini, F., Korte, M., Nilsson, A., Korhonen, K., Lodge, A., Lengyel, S.N. & Constable, C.G., 2015b. GEOMAGIA50. V3: 1. general structure and modifications to the archaeological and volcanic database, *Earth Planets Space,* **67,** 83, doi:10.1186/s40623-015-0232-0.

Brown, M.C., Korte, M., Holme, R., Wardinski, I. & Gunnarson, S., 2018. Earth's magnetic field is probably not reversing, *Proc. Natl. Acad. Sci. USA,* **115,** 5111–5116.

Cainelli, C., Babinski, N.A., Santos, R.C.R. & Uesugui, N., 1987. Sedimentos albo-santonianos da Bacia Sergipe-Alagoas: ambientes de sedimentação e perspectivas petrolíferas, *Rev. Bras. Geociê.,* **17,** 135–138.

Campos Neto, O.P.A., Lima, W.S. & Cruz, F.E.G., 2007. Bacia de Sergipe-Alagoas, *Bol. Geocienc Petrobras,* **15,** 405–415.

Chadima, M. & Hrouda, F., 2007. Remasoft 3.0 paleomagnetic Data browser and analyzer, http://www.agico.cz/text/software/remasoft/remasoft.php

Coe, R.S. & Glatzmaier, G.A. 2006. Symmetry and stability of the geomagnetic field, *Geophys. Res. Lett.,* **33**(21), 341–352.

Constable, C.G., Tauxe, L. & Parker, R.L., 1998. Analysis of 11 myr of geomagnetic intensity variation, *J. Geophys. Res. B: Solid Earth,* **103**(8), 17 735–17 748.

Cottrell, R.D. & Tarduno, J.A., 2000. In search of high-fidelity geomagnetic paleointensities: a comparison of single plagioclase crystal and whole rock Thellier-Thellier analyses, *J. geophys. Res.,* **105,** 23 579–23 594.

Cromwell, G., Johnson, C., Tauxe, L., Constable, C. & Jarboe, N., 2018. PSV10: a global data set for 0–10 ma time-averaged field and paleosecular variation studies, *Geochem. Geophys. Geosyst.,* **19,** 1533–1558.

Cronin, M., Tauxe, L., Constable, C., Selkin, P. & Pick, T., 2001. Noise in the quiet zone, *Earth Planet. Sci. Lett,* **190,** 13–30.

Day, R., Fuller, M. & Schmidt, V.A., 1977. Hysteresis properties of titanomagnetites; grain-size and compositional dependence, *Phys. Earth Planet Inter,* **13,** 260–267.

Dearing, J.A., Dann, R.J.L., Hay, K., Lees, J.A., Loveland, P.J., Maher, B.A. & O'Grady, K., 1996. Frequency-dependent susceptibility measurements of environmental materials, *Geophys. J. Int.,* **124,** 228–240.

de Groot, L.V., Biggin, A.J., Dekkers, M.J., Langereis, C.G. & Herrero-Bervera, E., 2013. Rapid regional perturbations to the recent global geomagnetic decay revealed by a new Hawaiian record, *Nat. Commun.,* **4,** doi:10.1038/ncomms3727.

Dembo, N., Kraus, E., Seliverstov, I., Weissman, G. & Granot, R., 2022. Geomagnetic field behaviour during the early cretaceous normal superchron from palaeomagnetic analysis of the Ramon Volcanics, Israel, *Geophys. J. Int.,* **231**(3), 1982–1995.

Di Chiara, A. *et al.*, 2021. Earth's magnetic field strength and the Cretaceous Normal Superchron: new data from Costa Rica, *Geochem. Geophys. Geosyst.,* **22**(4), e2020GC009605, doi:10.1029/2020GC009605.

Donadini, F., Korte, M. & Constable, C.G., 2009. Geomagnetic field for 0–3 ka: 1. New data sets for global modeling, *Geochem. Geophys. Geosyst.,* **10,** Q06007, doi:10.1029/2008GC002295.

Doubrovine, P.V., Veikkolainen, T., Pesonen, L.J., Piispa, E., Ots, S., Smirnov, A.V., Kulakov, E.V. & Beggin, A.J., 2019. Latitude dependence of geomagnetic paleosecular variation and its relation to the frequency of magnetic reversals: observations from the cretaceous and jurassic, *Geochem. Geophys. Geosyst.,* **20**(3), 1240–1279.

Driscoll, P. & Olson, P., 2011. Superchron cycles driven by variable core heat flow, *Geophys. Res. Lett.,* **38,** L09304, doi:10.1029/2011GL046808.

Dunlop, D.J., 2002a. Theory and application of the day plot (Mrs/Ms versus Hcr/Hc) 1. Theoretical curves and tests using titanomagnetite data, *J. Geophys. Res.,* **107**(B3), 2056, doi:10.1029/2001JB000486.

Dunlop, D.J., 2002b. Theory and application of the day plot (Mrs /Ms versus Hcr/Hc) 2. Application to data for rocks, sediments, and soils, *J. geophys. Res.,* **107**(B3), 2057, doi:10.1029/2001JB000487.

Dunlop, D.J. & Ozdemir, O., 1997. *Rock Magnetism: Fundamentals and Frontiers,* pp. 573, Cambridge Univ. Press, New York,

Egli, R., 2004. Characterization of individual rock magnetic components by analysis of remanence curves, 1. Unmixing natural sediments, *Stud. Geophys. Geod.,* **48,** 391–446.

Fauth, G. *et al.*, 2021. Drilling the Aptian–Albian of the Sergipe–Alagoas Basin, Brazil: paleobiogeographic and paleoceanographic studies in the South Atlantic, *Sci. Drill.,* **29,** 1–17.

Fauth, G. *et al.*, 2022. Astronomical calibration of the latest Aptian to middle Albian in the South Atlantic Ocean, *Palaeogeogr. Palaeoclimatol. Palaeoecol.,* **602,** 111175, doi:10.1016/j.palaeo.2022.111175.

Feijó, F.J., 1994. Bacias de Sergipe e Alagoas, *Bol. Geocienc Petrobras,* **8,** 149–161.

Feijó, F.J., 1996. O início da livre circulação das águas do Oceano Atlântico, *Bol. Geocienc Petrobras,* **10,** 157–164.

Font, E., Ernesto, M., Silva, P.A., Correia, P.B. & Nascimento, M.A.L., 2009. Palaeomagnetism, rock magnetism and AMS of the Cabo Magmatic Province, NE Brazil, and the opening of the South Atlantic, *Geophys. J. Int.,* **179,** 905–922.

Franco, D.R., de Oliveira, W.P., Freitas, F.B.V., Takahashi, D., Neto, C.F.P. & Peixoto, I.M.C., 2019. Paleomagnetic evidence for inverse correspondence between the relative contribution of the axial dipole field and CMB heat flux for the past 270 myr., *Sci. Rep.,* **9,** 282, doi:10.1038/s41598-018-36494-x.

Gilder, S.A., Chen, Y., Cogné, J.P., Tan, X., Courtillot, V., Sun, D. & Li, Y., 2003. Paleomagnetism of upper jurassic to lower cretaceous volcanic and sedimentary rocks from the western Tarim Basin and implications for inclination shallowing and absolute dating of the M-0 (ISEA?) chron, *Earth Planet. Sci. Lett.,* **206,** 587–600.

Glatzmaier, G.A., 2002. Geodynamo simulations: how realistic are they?, *Annu. Rev. Earth Planet. Sci.,* **30**(1), 237–257.

Glatzmaier, G.A., Coe, R.S., Hongre, L. & Roberts, P.H., 1999. The role of the Earth's mantle in controlling the frequency of geomagnetic reversals, *Nature,* **401,** 885–890.

Glatzmaier, G.A. & Roberts, P.H., 1995. A three-dimensional self-consistent computer simulation of a geomagnetic field reversal, *Nature,* **377**(6546), 203–209.

Gradstein, F.M., Ogg, J.G., Schmitz, M. & Ogg, G., 2020. *Geologic Time Scale 2020,* 1st edn., Elsevier. pp. 1390, doi:10.1016/C2020-1-02369-3.

Granot, R., Dyment, J. & Gallet, Y., 2012. Geomagnetic field variability during the cretaceous Normal Superchron, *Nat. Geosci.,* **5,** 220–223.

Guyodo, Y. & Valet, J.P., 1999. Global changes in geomagnetic intensity during the past 800 thousand years, *Nature,* **399,** 249–252.

He, H., Deng, C., Wang, P., Pan, Y. & Zhu, R., 2012. Toward age determination of the termination of the cretaceous Normal Superchron, *Geophys. Geochem. Geosyst.,* **13,** Q02002, G-Cubed, doi:10.1029/2011GC003901.

Helsley, C.E. & Steiner, M.B., 1968. Evidence for long intervals of normal polarity during the cretaceous period, *Earth Planet. Sci. Lett.,* **5,** 325–332.

Hill, M.J., Pan, Y. & Davies, C.J., 2008. An assessment of the reliability of palaeointensity results obtained from the cretaceous aged Suhongtu section, Inner Mongolia, China, *Phys. Earth Planet. Inter.,* **169,** 76–88.

Hounslow, M.W., Domeier, M. & Biggin, A.J., 2018. Subduction flux modulates the geomagnetic polarity reversal rate, *Tectonophysics,* **742–743,** 34–49.

Hrouda, F. & Pokorný, J., 2012. Modelling accuracy limits for frequency-dependent anisotropy of magnetic susceptibility of rocks and soils, *Stud. Geophys. Geod.,* **56,** 789–802.

Huber, B.T. & Leckie, R.M., 2011. Planktic foraminiferal species turnover across deep–sea Aptian/Albian boundary sections, *J. Foramin. Res.,* **41,** 53–95.

Huber, B.T., MacLeod, K.G., Gröcke, D.R. & Kucera, M., 2011. Paleotemperature and paleosalinity inferences and chemostratigraphy across the aptian/albian boundary in the subtropical North Atlantic, *Paleoceanography,* **26**(4), doi:10.1029/2011PA002178.

Hulot, G., Eymin, C., Langlais, B., Mandea, M. & Olsen, N., 2002. Small-scale structure of the geodynamo inferred from Ørsted and Magsat satellite data, *Nature,* **416,** 620–623.

Juárez, M.T., Tauxe, L., Gee, J.S. & Pick, T.,1998. The intensity of the Earth's magnetic field over the past 160 million years, *Nature,* **394,** 878–881.

Kageyama, A., Miyagoshi, T. & Sato, T., 2008. Formation of current coils in geodynamo simulations, *Nature,* **454**(7208), 1106–1109.

Kato, C., Sato, M., Yamamoto, Y., Tsunakawa, Y. & Kirschvink, J.L., 2018. Paleomagnetic studies on single crystals separated from the middle cretaceous Iritono granite, *Earth Planets Space,* **70,** 176, doi:10.1186/s40623-018-0945-y.

Keating, B.H. & Helsley, C.E., 1978. Paleomagnetic results from DSDP Hole 391C and the magnetostratigraphy of cretaceous sediments from the Atlantic Ocean floor, Vol. **44,** pp. 523–528, Benson, W.E. & Sheridan, R.E., eds, Government Printing Office, Washington, D.C., US.

Kennedy, J.W., Gale, A.s., Huber, B.T., Petrizzo, M.R., Bown, P. & Jenkyns, H.C., 2017. The global boundary stratotype section and point (GSSP) for the base of the albian stage, of the cretaceous, the Col de PréGuittard section, Arnayon, Drôme, France, *Episodes,* **40,** 177–188.

King, J., Banerjee, S.K. & Marvin, J., 1982. A comparison of different magnetic methods for determining the relative grain size of magnetite in natural materials: some results from lake sediments, *Earth Planet. Sci. Lett.,* **59,** 404–419p.

King, J.W., Banerjee, S.K., Marvin, J. & Lund, S., 1983. Use of small-amplitude paleomagnetic fluctuations for correlation and dating of continental climatic changes, *Palaeogeog. Palaeoclimatol. Palaeoecol.,* **42,** 167–183.

Kirschvink, J.L., 1980. The least-squares line and plane and the analysis of palaeomagneticdata, *Geophys. J. Roy. Astron. Soc.,* **62,** 699–718.

Kodama, K.P., 2012. *Paleomagnetism of Sedimentary Rocks,* 1st edn., pp. 94–123, John Wiley & Sons, Ltd, Chichester, UK

Korte, M., Brown, M.C., Panovska, S. & Wardinski, I., 2019. Robust characteristics of the Laschamp and Mono Lake geomagnetic excursions: results from global field models, *Front. Earth Sci.,* **7,** 427–447.

Koutsoukos, E.A.M., Mello, M.R. & Azambuja Filho, N.C., 1991a. Micropalaeontological and geochemical evidence of mid-cretaceous dysoxic-anoxic palaeoenvironments in the Sergipe Basin, northeastern Brazil, *Geol. Soc. Spec. Publ.,* **58,** 427–447.

Koutsoukos, E.A.M., Mello, M.R., Azambuja Filho, N.C., Hart, M.B. & Maxwell, J.R., 1991b. The upper aptian-albian succession of the Sergipe Basin, Brazil: an integrated paleoenvironmental assessment, *AAPG Bull.,* **75,** 479–498.

Kulakov, E.V. *et al.*, 2019. Analysis of an updated paleointensity database (QPI-PINT) for 65-200 ma: implications for the long-term history of dipole moment through the Mesozoic, *J. Geophys. Res.: Solid Earth,* **124,** 9999–10 022.

Larson, R.L. & Chase, C.G., 1972. Late mesozoic evolution of the Western Pacific ocean, *Geol. Soc. Am. Bull.,* **83**(12), 3627–3644.

Larson, R.L. & Olson, P., 1991. Mantle plumes control magnetic reversal frequency, *Earth Planet. Sci. Lett.,* **107**(3-4), 437–447.

Leandro, C.G. *et al.*, 2022. Astronomical tuning of the Aptian stage and its implications for age recalibrations and paleoclimatic events, *Nat. Commun.,* **13,** 2941, doi:10.1038/s41467-022-30075-3.

Leckie, R.M., Bralower, T.J. & Cashman, R. 2002. Oceanic anoxic events and plankton evolution: biotic response to tectonic forcing during the mid-Cretaceous, *Paleoceanography,* **17**(3), doi:.10.1029/2001PA00 0623

Levi, S. & Banerjee, S.K., 1976. On the possibility of obtaining relative paleointensities from lake sediments, *Earth Planet. Sci. Lett.,* **29,** 219–226.

Lhuillier, F. *et al.*, 2016. More stable yet bimodal geodynamo during the cretaceous superchron?, *Geophys. Res. Lett.,* **43**(12), 6170–6177.

Lhuillier, F. & Gilder, S.A., 2013. Quantifying paleosecular variation: insights from numerical dynamo simulations, *Earth Planet. Sc. Lett.,* **382,** 87–97.

Liu, Q., Roberts, A.P., Larrasoaña, J.C., Banerjee, S.K., Guyodo, Y., Tauxe, L. & Oldfield, F., 2012. Environmental magnetism: principles and applications, *Rev. Geophys.,* **50,** 1–50.

Liu, Q., Roberts, A.P., Torrent, J., Horng, C.-S. & Larrasoaña, J.C., 2007. What do the HIRM and S-ratio really measure in environmental magnetism?, *Geochem. Geophys. Geosyst.,* **8**(9), doi:10.1029/2007GC001717.

Liu, X., Li, Y.-X. & Richter, C., 2024. Salient changes of Earth's magnetic field toward the end of Cretaceous Normal Superchron (CNS), *J. Geophys. Res.: Solid Earth,* **129,** e2023JB028104, doi:10.1029/2023JB028104.

Luft-Souza, F., Fauth, G., Bruno, M.D.R., Mota, M.A.L., Vázquez-García, B., Santos Filho, M.A.B. & Terra, G.J.S., 2022. Sergipe-Alagoas Basin, Northeast Brazil: a reference basin for studies on the early history of the South Atlantic Ocean, *Earth Sci. Rev.,* **229,** 104 034., doi:10.1016/j.earscirev.2022.104034.

Lund, S., Benson, L., Negrini, R., Liddicoat, J. & Mensing, S., 2017. A full-vector paleomagnetic secular variation record (PSV) from Pyramid Lake (Nevada) from 47–17 ka: evidence for the successive Mono Lake and Laschamp excursions, *Earth Planet. Sci. Lett.,* **458,** 120–129.

Maxbauer, D.P., Feinberg, J.M. & Fox, D.L., 2016. MAX UnMix: a web application for unmixing magnetic coercivity distributions, *Comput. Geosci.,* **95,** 140–145.

McFadden, P.L. & Merrill, R.T., 1984. Lower mantle convection and geomagnetism, *J. Geophys. Res.,* **89**(B5), 3354–3362.

McFadden, P.L., Merrill, R.T., McElhinny, M.W. & Lee, S. 1991, Reversals of the Earth's magnetic field and temporal variations of the dynamo families, *J. Geophys. Res.,* **96,** 3923–3933.

Mello, M.R. & Katz, B.J., 2000. Petroleum systems of South Atlantic margins, *AAPG Mem.,* **73**.

Meynadier, L., Valet, J.P., Weeks, R., Shackleton, N. & Hagee, V.L., 1992. Relative paleointensities of the geomagnetic field during the last fourteen hundred thousand years, *Earth Planet. Sci. Lett.,* **114,** 39–57.

Muxworthy, A.R., Turney, J.N., Qi, L., Baker, E.B., Perkins, J.R. & Abdulkarim, M.A., 2023. Interpreting high-temperature magnetic susceptibility data of natural systems, *Front. Earth Sci.,* **11,** 1171 200.

Olierook, H.K.H., Jourdan, F., Whittaker, F., Merle, R.E., Jiang, Q., Pourteau, A. & Doucet, L.S., 2020. Timing and causes of the mid-cretaceous global plate reorganization event, *Earth Planet. Sci. Lett.,* **534,** 116 071.

Olson, P.L., Coe, R.S., Driscoll, P.E., Glatzmaier, G.A. & Roberts, P., 2010. H.Geodynamo reversal frequency and heterogeneous core-mantle boundary heat flow, *Phys. Earth Planet. Inter.,* **180,** 66–79.

Panovska, S., Korte, M. & Constable, C.G., 2019. One hundred thousand years of geomagnetic field evolution, *Rev. Geophys.,* **57,** 1289–1337.

Paterson, G.A., Heslop, D. & Yongxin, P., 2016. The pseudo-thellier palaeointensity method: new calibration and uncertainty estimates. GJI geomagnetism, rock magnetism and palaeomagnetism, *Geophys. J. Int.,* **207,** 1596–1608.

Pavón-Carrasco, F.J. & De Santis, A., 2016. The South Atlantic Anomaly: the key for a possible geomagnetic reversal, *Front. Earth Sci.,* **4,** 40, doi:10.3389/feart.2016.00040.

Ramos, J.M.F., Savia, J.F., Franco, D.R., Figueiredo, M.F., Leandro, C.G. & Frontalini, F., 2024. Orbital tuning of short reversed geomagnetic polarity intervals in the cretaceous Normal Polarity Superchron, *Geophys. Res. Lett.,* **51,** doi:10.1029/2024GL110530.

Roberts, A.P., Almeida, T.P., Church, N.S., Harrison, R.J., Heslop, D., Li, Y. & Zhao, X., 2017. Resolving the origin of pseudo-single domain magnetic behavior, *J. Geophys. Res. Solid Earth,***122,** 9534–9558.

Rodríguez-Trejo, A., Böhnel, H. & Ibarra-Ortega, H.E., 2024. LAPOD, Latin-American paleomagnetic online database: an online interface to access paleomagnetic data from Latin America, *J. South Am. Earth Sci.,* **145,** 105 060, doi:10.1016/j.jsames.2024.105060.

Ryan, W.B., Bolli, H.M., Foss, G.N., Natland, J.H., Hottman, W.E. & Foresman, J.B., 1978. Objectives, principal results, operations and explanatory notes of Leg 40, South Atlantic, *Init. Repts. DSDP,* **40,** 5–28.

Satolli, S., Besse, J., Speranza, F. & Calamita, F., 2008. Paleomagnetism of Aptian–Albian sections from the Northern Apennines (Italy): implications for the 150–100 ma apparent polar wander of Adria and Africa, *Earth Planet. Sci. Lett.,* **276,** 115–128.

Schaller, H., 1969. Revisão estratigráfica da Bacia de Sergipe/Alagoas, *Bol. Téc. Petrobras,* **12,** 21–86.

Shcherbakov, V.V., Bakhmutov, V.G., Thallner, D., Shcherbakov, V.P., Zhidkov, G.V. & Biggin, A.J., 2020. Ultra-low palaeointensities from East European Craton, Ukraine support a globally anomalous palaeomagnetic field in the Ediacaran, *Geophys. J. Int.,* **220**(2020), 1920–1946.

Shcherbakova, V.V., Kovalenco, D.V., Shcherbakov, V.P. & Zhidkov., G.V., 2011. Paleointensity of the geomagnetic field in the Cretaceous (from Cretaceous rocks of Mongolia), *Izv. Phys. Solid Earth,* **47,** 775–791.

Shi, R., He, H., Zhu, R. & Pan, Y., 2004. ISEA reversed event in the cretaceous normal Super-chron (CNS): 40Ar/39Ar dating and paleomagnetic results, *Chin. Sci. Bull.,* **49**(9), 926–930.

Tarduno, J.A., 1990. Brief reversed polarity interval during the cretaceous normal polarity superchron, *Geology,* **18**(8), 683–686.

Tarduno, J.A., Cottrell, R.D. & Smirnov, A.V., 2001. High geomagnetic field intensity during the mid-cretaceous from Thellier analyses of single plagioclase crystals, *Science,* **291**(5509), 1779–1783.

Tarduno, J.A., Cottrell, R.D. & Smirnov, A.V., 2002. The cretaceous superchron geodynamo: observations near the tangent cylinder, *Earth Atmos. Planet. Sci.,* **99**(22), 14 020–14 025.

Tauxe, L., 1993. Sedimentary records of relative paleointensity of the geomagnetic field: theory and practice, *Rev. Geophys.,* **31,** 319–354.

Tauxe, L., 2006. Long-term trends in paleointensity: the contribution of DSDP/ODP submarine basaltic glass collections, *Phys. Earth Planet. Inter.,* **156**(3–4), 223–241.

Tauxe, L., Gee, J.G., Steiner, M.B. & Staudigel, H., 2013. Paleointensity results from the Jurassic: new constraints from submarine basaltic glasses of ODP Site 801C, *Geochem. Geophys. Geosyst.,* **14,** 10, doi:10.1002/ggge.20282.

Tauxe, L. & Hartl, P., 1997. 11 million years of oligocene geomagnetic field behaviour, *Geophys. J. Int.,* **128,** 217–229.

Tauxe, L., Pick, T. & Kok, Y.S., 1995. Relative paleointensity in sediments: a Pseudo-Thellier approach, *Geophys. Res. Lett.,* **22,** 2885–2888.

Thompson, R. & Oldfield, F., 1986. *Environmental Magnetism,* pp. 225, Allen & Unwin Ltd.

Torsvik, T.H. *et al.*, 2012. Phanerozoic polar wander, palaeogeography and dynamics, *Earth Sci. Rev.,* **114**(3-4), 325–368.

Tsunakawa, H., Wakabayashi, K.I., Mochizuki, N., Yamamoto, Y., Ishizaka, K., Hirata, T., Takahashi, F. & Seita, K., 2009. Paleointensity study of the middle cretaceous Iritono granite in northeast Japan: implication for high field intensity of the cretaceous normal superchron, *Phys. Earth Planet. Inter.,* **176**(3), 235–242.

Valet, J.-P., Thevarasan, A., Bassinot, F., Savranskaia, T. & Haddam, N., 2020. Two records of relative paleointensity for the past 4 myr, *Front. Earth Sci.,* **8,** 148.

Vandenberg, J., Klootwijk, C.T. & Wonders, A.A.H., 1978. The late mesozoic and cenozoic movements of the Umbrian Peninsula: further palaemagnetic data from the Umbrian Sequence, *Geol. Soc. Am. Bull.,* **89,** 133–150.

Whaler, K.A. & Holme, R., 2011. The axial dipole strength and flow in the outer core, *Phys. Earth Planet. Inter.,* **188**(3–4), 235–246.

Yamamoto, Y. & Tsunakawa, Y. 2005. Geomagnetic field intensity during the last 5 myr: LTD-DHT Shaw palaeointensities from volcanic rocks of the Society lslands, French Polynesia, *Geophys. J. Int.,* **162,** 79–114.

Yamamoto, Y., Yamazaki, T., Kanamatsu, T., Ioka, N. & Mishima, T., 2007. Relative paleointensity stack during the last 250 kyr in the northwest Pacific, *J. Geophys. Res.: Solid Earth,* **112**(B01104), doi:10.1029/2006JB004477.

Yamazaki, T., Kanamatsu, T., Mizuno, S., Hokanishi, N. & Gaffar, E.Z., 2008. Geomagnetic field variations during the last 400 kyr in the western equatorial Pacific: paleointensity-inclination correlation revisited, *Geophys. Res. Lett,* **25,** 20, doi:10.1029/2008GL035373.

Yamazaki, T. & Oda, H., 2005. A geomagnetic paleointensity stack between 0.8 and 3.0 ma from equatorial Pacific sediment cores, *Geochem. Geophys. Geosystem.,* **6,** 11, doi:10.1029/2005GC001001.

Yamazaki, T. & Yamamoto, Y., 2014. Paleointensity of the geomagnetic field in the late Cretaceous and earliest Paleogene obtained from drill cores of the Louisville seamount trail, *Geochem. Geophys. Geosyst.,* **15,** 6, doi:10.1002/2014GC005298.

Yoshimura, Y., 2022. The cretaceous normal Superchron: a mini-review of its discovery, short reversal events, paleointensity, paleosecular variations, paleoenvironment, volcanism, and mechanism, *Front. Earth Sci.,* **10,** doi:10.10.3389/feart.2022.834024.

Yoshimura, Y., Yamazaki, T., Yamamoto, Y., Ahn, H.S., Kidane, T. & Otofuji, Y., 2020. Geomagnetic paleointensity around 30 ma estimated from Afro-Arabian large igneous province, *Geochem. Geophys. Geosystems,* **21**(12), doi:10.1029/2020GC009341.

Zhang, D., Yan, M., Song, C., Zhang, W., Fang, X. & Li, B., 2021. Frequent polarity reversals in the cretaceous Normal Superchron, *Geophys. Res. Lett.,* **48,** 5, doi:10.1029/2020GL091501.

Zhu, R., Pan, Y., He, H., Qin, H. & Ren, S., 2008. Paleomagnetism and 40Ar/39Ar age from a cretaceous volcanic sequence, Inner Mongolia, China: implications for the field variation during the cretaceous normal superchron, *Phys. Earth Planet. Inter.,* **169,** 59–75.

Zijderveld, J.D.A., 1967. AC Demagnetization of Rocks: Analysis of Results, Runcorn,, S.K., Creer,, K.M. & Collinson,, D.W., *Methods in Paleomagnetism,* Vol. **3** Elsevier, Amsterdam. 254–286.